Becherer, J.; Moum, J.; Calantoni, J.; Colosi, J.; Barth, J.; Lerczak, J.; McSweeney, J.; MacKinnon, J.; Waterhouse, A.:

Saturation of the Internal Tide over the Inner Continental Shelf. Part II: Parameterization.

In: Journal of Physical Oceanography. Vol. 51 (2021) 8, 2565 - 2582.

First published online by AMS: 22.07.2021

https://dx.doi.org/10.1175/JPO-D-21-0047.1

Saturation of the Internal Tide over the Inner Continental Shelf. Part II: Parameterization

JOHANNES BECHERER,[a,b] JAMES N. MOUM,[a] JOSEPH CALANTONI,[c] JOHN A. COLOSI,[d] JOHN A. BARTH,[a] JAMES A. LERCZAK,[a] JACQUELINE M. MCSWEENEY,[a] JENNIFER A. MACKINNON,[e] AND AMY F. WATERHOUSE[e]

[a] *College of Earth, Ocean, and Atmospheric Sciences, Oregon State University, Corvallis, Oregon*
[b] *Institute of Coastal Research, Helmholtz-Zentrum Hereon, Geesthacht, Germany*
[c] *Ocean Sciences Division, U.S. Naval Research Laboratory, Stennis Space Center, Mississippi*
[d] *Department of Oceanography, Naval Postgraduate School, Monterey Bay, California*
[e] *Scripps Institution of Oceanography, University of California, San Diego, La Jolla, California*

(Manuscript received 2 March 2021, in final form 26 April 2021)

ABSTRACT: Here, we develop a framework for understanding the observations presented in Part I. In this framework, the internal tide saturates as it shoals as a result of amplitude limitation with decreasing water depth H. From this framework evolves estimates of averaged energetics of the internal tide; specifically, energy $\langle \mathrm{APE} \rangle$, energy flux $\langle F_E \rangle$, and energy flux divergence $\partial_x \langle F_E \rangle$. Since we observe that dissipation $\langle D \rangle \approx \partial_x \langle F_E \rangle$, we also interpret our estimate of $\partial_x \langle F_E \rangle$ as $\langle D \rangle$. These estimates represent a parameterization of the energy in the internal tide as it saturates over the inner continental shelf. The parameterization depends solely on depth-mean stratification and bathymetry. A summary result is that the cross-shelf depth dependencies of $\langle \mathrm{APE} \rangle$, $\langle F_E \rangle$, and $\partial_x \langle F_E \rangle$ are analogous to those for shoaling surface gravity waves in the surf zone, suggesting that *the inner shelf is the surf zone for the internal tide*. A test of our simple parameterization against a range of datasets suggests that it is broadly applicable.

SIGNIFICANCE STATEMENT: Observational results from Part I suggest a new approach to understanding the complicated breakdown of the internal tide over continental shelves. By defocusing on the details in favor of focusing on the integral energy of the internal tide, we develop a new framework analogous to breaking surface waves on beaches. This framework leads to a simple parameterization that depends solely on the surface-to-seafloor temperature difference and the bathymetry of the continental shelf. A test of this parameterization against a range of datasets shows broad applicability. At the same time, it provides a means of determining the net mixing of continental shelf waters and suggests that the inner continental shelf is the *surf zone for the internal tide.*

KEYWORDS: Ocean; Continental shelf/slope; Baroclinic flows; Coastal flows; Diapycnal mixing; Internal waves; Mixing; Solitary waves; Transport; Turbulence; Wave breaking; Waves, oceanic; Energy transport; Tides; In situ oceanic observations; Parameterization

1. Introduction

The inner continental shelf, the transition zone between midshelf and surf zone, can be characterized as the region where surface and bottom boundary layer overlap (Lentz 1994). Alternatively, it is the region where cross-shore winds significantly contribute to cross-shelf transport; this is in contrast to the unbound Ekman dynamics of the midshelf (Fewings et al. 2008). However, it is also the place where the internal tide dissipates almost all of its energy, a point that has found less attention as a defining feature of the inner shelf. Here we focus on this particular aspect and develop a conceptual framework that suggests a new perspective on the inner shelf's role as the surf zone for the internal tide (section 5a). This *internal* surf zone, in which the bulk-averaged internal tide exists in a saturated state confined by the water depth, has features analogous to the surf zone for surface gravity waves (Thornton and Guza 1983; Sallenger and Holman 1985; Battjes 1988).

Generation of the internal tide happens both locally at the shelf break (Sharples et al. 2001; Duda and Rainville 2008; Kang and Fringer 2010) and at remote locations—hundreds to thousands of kilometers away (Alford et al. 2007; Nash et al. 2012; Kumar et al. 2019). The shoaling internal tide can provide a significant fraction of the inner shelf's energy (Moum et al. 2007b; Kang and Fringer 2012). Here the internal tide's energy is dissipated causing turbulence and diapycnal mixing. Inside the inner shelf region the internal tide significantly contributes to cross-shelf transport of energy (Moum et al. 2007a), heat (Gough et al. 2020), mass (Shroyer et al. 2010b), sediment (Butman et al. 2006; Pomar et al. 2012; Boegman and Stastna 2019; Becherer et al. 2020), nutrients (Sandstrom and Elliott 1984; Sharples et al. 2007), and biomass (Scotti and Pineda 2007).

Understanding the shoaling dynamics and eventual dissipation of the internal tide on the shelf is a challenging research question and the focus of many past studies (Helfrich and Melville 2006). Because of nonlinear interactions, the internal tide usually appears on the inner shelf as a complex superposition of a multitude of different nonlinear internal wave (NLIW) forms with frequencies ranging from the tidal forcing frequency to the buoyancy frequency N (McSweeney et al. 2020b). Much progress has been made in understanding the shoaling behavior of individual NLIWs in idealized theoretical

Corresponding author: Johannes Becherer, johannes.becherer@hereon.de

DOI: 10.1175/JPO-D-21-0047.1

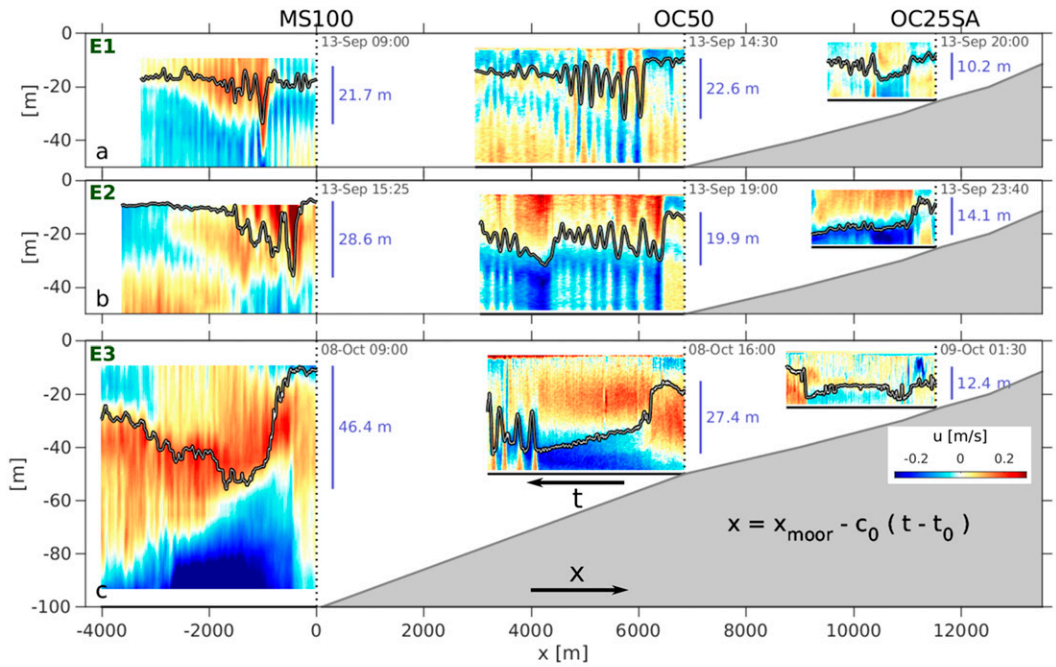

FIG. 1. Three examples of shoaling internal tide signals from the ISDE that can be tracked onshore from data at three moorings at isobaths 100, 50, and 25 m across the shelf. Corresponding time series of velocity, temperature, and dissipation rate can be found in Part I (E1 and E2 in Fig. 4 of Part I; E3 in Fig. 5 of Part I). The onshore component of the current velocity is image colored; the black/white lines show the isotherms closest to the vertical position of peak stratification in the water column. Measured time series at moorings are converted to space with $x = x_{\mathrm{moor}} - c_0(t - t_0)$, where x_{moor} is the mooring's position on a cross-shelf transect, c_0 the linear mode-1 phase speed [see (9)], and t_0 is the start time of each event. For each event, t_0 is written to the right of the dashed vertical line that marks x_{moor}. Because of the convention used here, x and t increase in opposite directions as indicated by the black arrows in (c). The blue vertical line ahead of each event indicates the maximum isothermal displacement.

(e.g., Holloway et al. 1999; Grimshaw et al. 2004), laboratory (Boegman et al. 2005; Boegman and Ivey 2009; Carr et al. 2008), and numerical studies (e.g., Vlasenko and Hutter 2002; Kang and Fringer 2010; Venayagamoorthy and Fringer 2007; Lamb 2014) as well as detailed process-orientated observational studies (e.g., Inall et al. 2000; Klymak and Moum 2003; Moum et al. 2003, 2007a; Scotti et al. 2008; Bourgault et al. 2008; Shroyer et al. 2010a; Walter et al. 2014; Becherer et al. 2020).

Several different mechanisms have been identified by which the internal tide and NLIWs dissipate their energy while propagating across the shelf (Lamb 2014). These include direct breaking at steep slopes (Klymak et al. 2011; Arthur and Fringer 2014) and at the point where the waveguide intersects the bottom (Vlasenko and Hutter 2002; Aghsaee et al. 2010; Lamb 2014). The breaking mechanisms can differ depending (for instance) on the ratio between bottom and isopycnal slope, quantified by the Iribarren number ξ (Vlasenko and Hutter 2002; Boegman et al. 2005). Four different breaking regimes are identified: surging, collapsing, plunging, and fission. Aghsaee et al. (2010) argues that for most oceanic shelves with their comparably shallow slopes (<0.01) fission is the most important process. After breaking, some part of the NLIWs can potentially propagate beyond the point where the pycnocline intersects with the bottom in small wave packets of elevation with trapped cores or boluses (Venayagamoorthy and Fringer 2007; Bourgault et al. 2008; Walter et al. 2012, 2014). In addition to catastrophic breaking, the NLIWs associated with the internal tide also gradually dissipate energy while shoaling. This can either happen at the pycnocline due to shear instabilities (Bogucki and Garrett 1993; Sandstrom and Oakey 1995; Moum et al. 2003; Barad and Fringer 2010; Lamb and Farmer 2011) or at the bottom due to frictional interaction with the bed (Bogucki and Redekopp 1999; Stastna and Lamb 2002; Rippeth and Inall 2002; Boegman and Stastna 2019; Becherer et al. 2020).

In Figs. 4 and 5 of Becherer et al. (2021, hereinafter Part I) we showed that the shoaling internal tide appears in many different wave configurations, ranging from trains of high-frequency internal waves of both elevation and depression over almost rectangular-shaped bore fronts, to gentle low-frequency waves. A few randomly chosen examples of internal tide features that can be traced across several moorings as the tidal signal propagates from the 100-m isobath through 50 m to 25 m are illustrated in Fig. 1. More examples can be found in McSweeney et al. (2020a,b), Kumar et al. (2021), and Becherer et al. (2020). Besides the energy in and shape of the incident tidal signal, its evolution across the shelf is dictated by bathymetry, stratification and background currents. Except for bathymetry these factors can change on relatively short time scales, where preceding bore fronts influence the background state trailing bores propagating into (McSweeney et al. 2020b), which can also substantially change with along-shelf location (McSweeney et al. 2020a). This chaotic interaction between successive wave fronts makes it potentially impossible to predict the exact development of a particular tidal signal across the shelf.

Despite the complexities of interaction and evolution that compose the shoaling internal tide, we were able to extract several major findings in Part I. By studying the internal tide and its properties in an average sense, where our averaging window (36 h) was chosen such that it contains an ensemble of internal tide forms (see Figs. 4 and 5 in Part I) we find that

- the internal tide dissipates most of its energy between the 100 and 20-m isobath;
- as the internal tide shoals, the energy flux at shallower sites becomes progressively decorrelated from the offshore incident wave energy;
- stratification is the controlling factor in determining the relative magnitude of internal tidal energy tunneled to shallower sites; and
- internal tide energy levels over the inner shelf can be completely independent of offshore energy levels, thus indicating that the internal tide loses the memory of its initial strength as it shoals.

This latter point suggests that it is possible to predict internal tide energy levels over the inner shelf with little, and mainly local, information. Testing this hypothesis is the primary objective of this paper.

Our strategy here is to neglect the hierarchical complexities of the internal tide propagating across the inner shelf and develop a practical framework to describe the internal tide's shoaling behavior in a bulk-averaged sense. We use averaged energetic considerations that are largely independent of wave type or frequency. By doing so we employ a very different approach than previous process-oriented studies that concentrated on understanding the important problems associated with the shoaling behaviors of individual waves. This bulk-averaged approach leads to a holistic description of the internal tide's dissipation over the shelf.

To this end we introduce a new conceptual framework that assumes the internal tide reaches a state of energy saturation over the inner shelf (section 2). Based on this framework we construct simple parameterizations for energy, energy flux, and flux divergence (that we take to be equivalent to the energy dissipated by turbulence) of the internal tide over the inner shelf that depends only on mean background stratification and bathymetry (section 2d). An evaluation of this parameterization by comparison with our direct measurements is done in section 2g. We consider implications of this result in section 3 and demonstrate that our new parameterization quantitatively reproduces results from a range of previous studies (section 4), thus suggesting general applicability. It also suggests a new additional definition of the inner shelf as the region of the saturated internal tide.

The saturation framework provides an accounting for the interesting correlations found in Part I, mentioned above

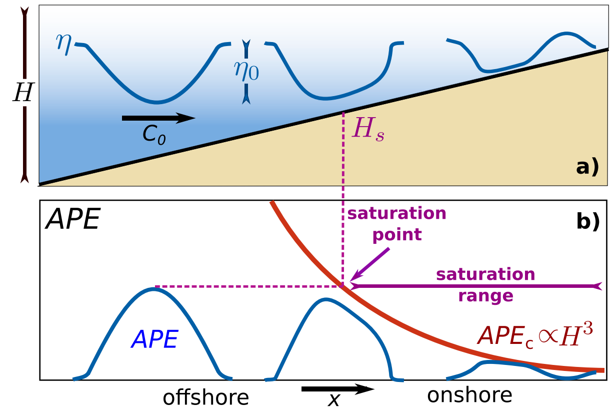

FIG. 2. Schematic of an idealized shoaling internal wave. (a) During shoaling the water depth decreases. At some point H_S the water depth becomes comparable to the amplitude of the internal wave. Inshore from this point the water depth is the effective limit for the amplitude of the internal wave, such that the amplitude has to decrease in order for the internal wave to be able to propagate into the saturated range. (b) Since the amplitude of the internal wave is related to the APE through (4), the upper bound for η_0 translates into an upper bound for the available potential energy, APE_c, that is proportional to H^3 [see (5)].

(sections 5b and 5c) and further insights into internal tide dynamics over the inner shelf, including a prediction of the cross-shore location of maximum dissipation (section 5e), a formulation of the dissipation length scale (section 5f), and hints toward a mixing feedback mechanism (section 5d). A summary and conclusions follow (section 6).

2. Saturated internal tide

a. Concept

Figure 2 conceptually illustrates the shoaling process of an idealized first-mode internal wave. The internal wave propagates shoreward with isopycnal displacement η. As the wave shoals, the amplitude η_0 becomes comparable to the water depth H. At some point H imposes an effective upper bound on η_0 such that η_0 must decrease to propagate into shallower waters (Fig. 2a).

The magnitude of η largely defines the local available potential energy (APE; Winters et al. 1995). Water depth and stratification limit the maximum available potential energy APE_c. This maximum capacity decreases rapidly with water depth ($\propto H^3$). A shoaling internal tide must lose energy to follow the restrictions set by APE_c (Fig. 2b).

It is important to note that the schematic wave depicted in Fig. 2a does not show the internal tide's complexity seen in Fig. 1. It is intended as a statement that the common feature of the wave hierarchy is that their individual amplitudes determine their maximum APE. The schematic serves as guidance for describing the shoaling of the internal tide in a bulk-averaged sense, while disregarding its complexity.

We term the water depth at which the shoaling internal tide is, on average, first influenced by the water column's energy restriction the *saturation water depth* H_s and the region inshore of H_s the *saturated range* (SR). In the following, we develop an expression for APE_c that is then used to develop a parameterization for energy, energy flux, and flux divergence of the bulk-averaged internal tide within the SR.

b. Available potential energy

The available potential energy density of internal waves can be expressed as (Nash et al. 2005; Kang and Fringer 2010)

$$\mathrm{ape} = \frac{g^2}{2\rho_0}\frac{\rho'^2}{\langle N^2\rangle} = \frac{1}{2}\rho_0\langle N^2\rangle\eta^2 \quad (\mathrm{J\ m^{-3}}), \tag{1}$$

where angle brackets denote a 36-h low-pass filter, $\rho' = \rho - \langle\rho\rangle$ is a density perturbation, ρ_0 is a constant reference density, and $g = 9.81\ \mathrm{m\,s^{-2}}$ the gravitational acceleration.

The background stratification is defined as

$$\langle N^2\rangle = -\frac{g}{\rho_0}\frac{d\langle\rho\rangle}{dz} \quad (\mathrm{s^{-2}}), \tag{2}$$

and the isopycnal displacement of the internal wave field is

$$\eta = \frac{g}{\rho_0\langle N^2\rangle}\rho'. \tag{3}$$

The water column–integrated available potential energy is

$$\mathrm{APE} = \int_0^H \mathrm{ape}\,dz = \frac{1}{2}\rho_0\int_0^H\langle N^2\rangle\eta^2\,dz \quad (\mathrm{J\ m^{-2}}). \tag{4}$$

The total depth-integrated energy is then defined as $E = \mathrm{APE} + \mathrm{KE}$, where KE is the kinetic energy component.

c. Energy capacity

The water depth and stratification determine the upper bound to APE as follows. The maximum downward isopycnal displacement is restricted by the distance to the bottom, $\eta_{\max D} = -z$, and the corresponding maximum elevation is restricted by the distance to the surface, $\eta_{\max E} = H - z$.

Using either $\eta_{\max D}$ or $\eta_{\max E}$ in (4) yields the identical expression for the maximum capacity:

$$\mathrm{APE}_c = \frac{1}{2}\rho_0\langle\overline{N^2}\rangle\int_0^H\eta_{\max}^2\,dz = \frac{1}{6}\rho_0\langle\overline{N^2}\rangle H^3, \tag{5}$$

with

$$\langle\overline{N^2}\rangle = \frac{1}{H}\int_0^H\langle N^2\rangle\,dz = -\frac{g}{\rho_0}\frac{\langle\Delta\rho\rangle}{H}, \tag{6}$$

where $\langle\Delta\rho\rangle$ denotes the mean top-to-bottom density difference.

Using $\langle\overline{N^2}\rangle$ in (5) instead of $\langle N^2\rangle$ appears as a simplification at first, but it implicitly incorporates large-amplitude corrections for (4), because it corresponds to an average of $\langle N^2\rangle$ over the full extent of maximum isopycnal displacement (i.e., the entire water column). Analogous to (5) it is possible to derive a maximum capacity for the kinetic energy, which is demonstrated in the appendix.

d. Parameterization

From (5), we develop a parameterization for the mean available potential energy of the internal tide inside the SR:

$$\mathrm{APE}^{\mathrm{par}} = C_A\mathrm{APE}_c = \frac{C_A}{6}\rho_0\langle\overline{N^2}\rangle H^3, \tag{7}$$

where C_A is a proportionally factor. The available potential energy is related to the baroclinic energy flux (Moum et al. 2007b),

$$\langle F_E\rangle = C_F c_g\langle\mathrm{APE}\rangle, \tag{8}$$

where C_F is a proportionally factor. For long waves in shallow water the group speed c_g is approximated to first order by the linear phase speed c_0. The linear phase speed for first-vertical-mode waves in constant stratification is

$$c_0 = \frac{1}{\pi}\langle\overline{N^2}\rangle^{1/2}H. \tag{9}$$

Equations (7) and (9) lead to a parameterization for $\langle F_E\rangle$ inside the SR,

$$F_E^{\mathrm{par}} = C_F C_A c_0\mathrm{APE}_c = \frac{C_F C_A}{6\pi}\rho_0\langle\overline{N^2}\rangle^{3/2}H^4. \tag{10}$$

The proportionality factors C_A and C_F, are yet to be determined.

The x derivative of (10) yields an expression for the flux divergence,

$$\partial_x F_E^{\mathrm{par}} = C_{Fx}\frac{2C_F C_A}{3\pi}\rho_0\langle\overline{N^2}\rangle^{3/2}H^3\partial_x H \quad (\mathrm{W\ m^{-2}}), \tag{11}$$

with

$$C_{Fx} = 1 + \frac{3}{8}\frac{H}{\langle\overline{N^2}\rangle}\frac{\partial_x\langle\overline{N^2}\rangle}{\partial_x H}. \tag{12}$$

The second term on the right-hand-side of (12) factors in a potential x dependence of $\langle\overline{N^2}\rangle$ into (11).

To estimate C_{Fx} we consider two limiting cases:

1) for spatially uniform stratification, $\partial_x\langle\overline{N^2}\rangle = 0$, and $C_{Fx} = 1$;
2) in the case of a pycnocline sufficiently far away from the seafloor so that $\partial_x\Delta\rho = 0$ in (6), $\partial_x\langle\overline{N^2}\rangle = -\langle\overline{N^2}\rangle H^{-1}\partial_x H$, which yields $C_{Fx} = 5/8$.

For most scenarios we expect $5/8 < C_{Fx} < 1$, where C_{Fx} is likely to be smaller in deep waters than in shallow waters, where the pycnocline is closer to the seafloor.

e. Free parameters

To use the parameterizations (7)–(11), we require estimates of the proportionality factors C_A and C_F. Factor C_A is the ratio of low-pass-filtered (36 h) available potential energy of the internal tide $\langle\mathrm{APE}\rangle$ to APE_c, which can be related as

$$C_A = \frac{\mathrm{APE}^{\max}}{\mathrm{APE}_c}\frac{\langle\mathrm{APE}\rangle}{\mathrm{APE}^{\max}}. \tag{13}$$

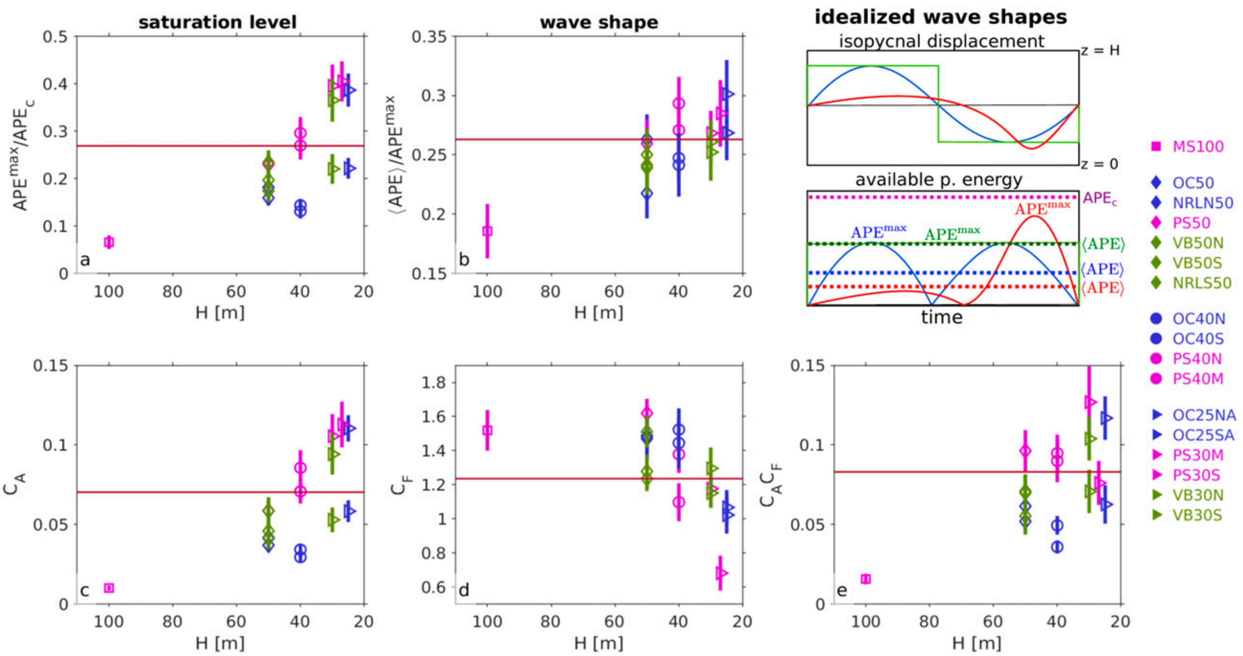

FIG. 3. Estimates of proportionality factors that appear in (7)–(11): (a) saturation level, (b) shape factor, (c) C_A, (d) C_F, and (e) the product C_AC_F. The symbols indicate the 2-month average for each mooring with corresponding error bars (for mooring positions, see Fig. 1 in Part I). The red lines are average values across the entire mooring array, excluding MS100 (leftmost symbol). The two panels at upper right show idealized wave shapes and corresponding maximum and mean APE in relation to APE_c.

The first factor in (13), the ratio of the maximum available potential energy in a tidal cycle $\mathrm{APE}^{\max}$ to APE_c, is a measure of the level of saturation. The saturation level ranges from ≈0.2 at $H = 50$ m to 0.4 at the shallow moorings (Fig. 3a). Excluding mooring MS100, the average saturation level is 0.27 (Table 1).

The second factor in (13), $\langle\mathrm{APE}\rangle/\mathrm{APE}^{\max}$, is related to the shape of the internal tide. For rectangular waves, the shape factor is 1, for sine waves it is 0.5, and for intermittent more-complicated asymmetric wave forms it is < 0.5 (Fig. 3). In general, the shape factor is approximated by

$$\frac{\langle\mathrm{APE}\rangle}{\mathrm{APE}^{\max}} = \frac{1/T\int_T \eta^2\,dt}{\eta^2_{\max}}. \tag{14}$$

Excluding MS100, the mean value of the shape factor is 0.26 (Fig. 3b, Table 1).

The product of the saturation level and the shape factor yields $C_A = 0.07$ (Fig. 3c), implying that inside the SR the $\langle\mathrm{APE}\rangle$ is roughly 7% of the maximum capacity APE_c.

Factor C_F is the proportionality factor in (8). It is difficult to predict C_F theoretically. For freely propagating linear waves, the kinetic and available potential energy relate as $\langle\mathrm{KE}\rangle/\langle\mathrm{APE}\rangle = (\omega^2 + f^2)/(\omega^2 - f^2)$, where the wave's frequency is ω and the Coriolis frequency is f. For a monochromatic wave with M_2 tidal frequency at our latitude, we get $\langle\mathrm{KE}\rangle/\langle\mathrm{APE}\rangle = 2.2$, corresponding to $C_F = 1 + \langle\mathrm{KE}\rangle/\langle\mathrm{APE}\rangle = 3.2$. For waves that are close to a lateral boundary (steep slope or coast), the ratio will be very different because of backward reflection of the incident wave (Nash et al. 2004; Waterhouse et al. 2017). In addition, during the shoaling process the internal tide steepens and becomes increasingly nonlinear, which results in higher harmonics as well as the generation of high-frequency undular bores. Even the first harmonic M_4 yields with the above formula $\langle\mathrm{KE}\rangle/\langle\mathrm{APE}\rangle \approx 1$, and Moum et al. (2007b) show that packets of high-frequency internal solitons have an equal partitioning between available potential and kinetic energy, which would result in $C_F = 2$.

From the mooring data, we find on average $C_F = 1.23$ (Table 1), with some apparent depth dependence, where C_F decreases from about 1.5 at $H = 50$ m to about 1.0 at $H = 25$ m (Fig. 3d). Despite being on average shoreward directed, we find brief periods during each tidal cycle in which the instantaneous flux is offshore directed (see Fig. 6 in Part I). This indicates that reflection may play a significant role in altering C_F. If we ignore direction and just average the sole magnitude of $|F_E|$, we find an average ratio $\langle|F_E|\rangle/(c_0\langle\mathrm{APE}\rangle) \approx 1.8$ (red dots in Fig. 4), which is closer to 2—the value expected for a wave of equally partitioned KE and APE traveling in one direction.

TABLE 1. List of parameters evaluated from the observations (Fig. 3) as input to the parameterizations (7)–(11).

Parameter	Relation	Figure panel	Value
$\mathrm{APE}^{\max}/\mathrm{APE}_c$	Saturation level	Fig. 3a	0.27
$\langle\mathrm{APE}\rangle/\mathrm{APE}^{\max}$	Wave shape	Fig. 3b	0.26
C_A	$\langle\mathrm{APE}\rangle/\mathrm{APE}_c$	Fig. 3c	0.070
C_F	$F_E/(c_0\langle\mathrm{APE}\rangle)$	Fig. 3d	1.23
C_FC_A	$F_E/(c_0\mathrm{APE}_c)$	Fig. 3f	0.083

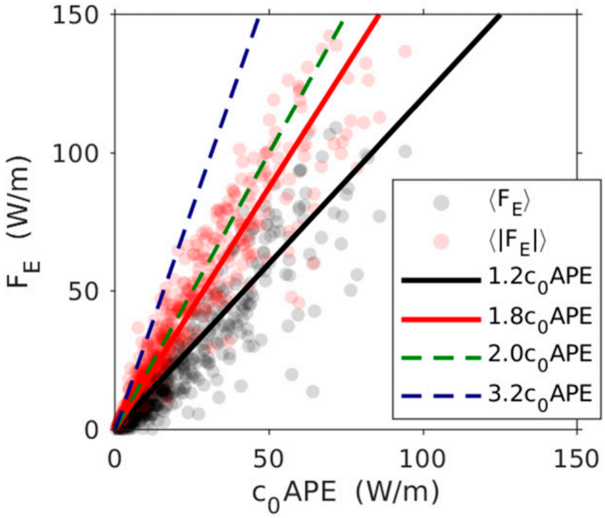

FIG. 4. Scatterplot of the flux coefficient C_F for every 36-h window at all mooring sites, excluding MS100. Black dots represent averages of the onshore component of $\langle F_E \rangle$, and red dots are averages of the magnitude $\langle |F_E| \rangle$ regardless of direction. The black line corresponds to $C_F = 1.23$, which is the best fit for black dots. The best fit for red dots (red line) has a slope of 1.8. As reference, we plot a slope of 2 (green dashed line), corresponding to a unidirectional wave with an equal partition between APE and KE, and a slope of 3.2 (blue dashed line), corresponding to a freely propagating M_2 tide at our latitude.

f. Saturation depth H_s

The parameterization (7)–(11) is only valid inside the SR (Fig. 2). The SR is defined by a characteristic water depth H_s inshore of which the internal tide is saturated. To calculate H_s, we set the incoming baroclinic energy flux $\langle F_E^{\text{in}} \rangle$ equal to F_E^{par} in (10) and solve for H, which yields

$$H_s = \left[\frac{6\pi}{C_A C_F \rho_0}\right]^{1/4} \langle \overline{N^2} \rangle^{(-3/8)} \langle F_E^{\text{in}} \rangle^{1/4}. \tag{15}$$

Using the mean baroclinic energy flux at MS100 as a measure of $\langle F_E^{\text{in}} \rangle = \langle F_E \rangle|_{\text{MS100}}$, we find that H_s varies between 40 and 80 m, with an average value of $H_s = 58.4$ (Fig. 5). This indicates that all moorings, except for MS100, are inside the SR most of the time. MS100, on the other hand, is always outside the SR during the 2-month-long observation period.

Depth H_s is a crucial parameter to determine whether the parameterization (7)–(11) can be applied to a particular dataset. If (7)–(11) strongly overestimate the average measurement at a particular mooring site, it suggests that the mooring lies outside the SR. In this case locally measured $\langle F_E \rangle$ can be used as an input for (15) to determine the extent of the saturated range. On the other hand, if (7)–(11) do not overestimate local measurements, it can be assumed that the corresponding mooring already lies within the SR. In this case, it is not possible to determine the offshore extend of the SR solely on the basis of measurements of this single mooring. It is fair, however, to assume that (7)–(11) are a valid parameterization inshore of the given mooring location.

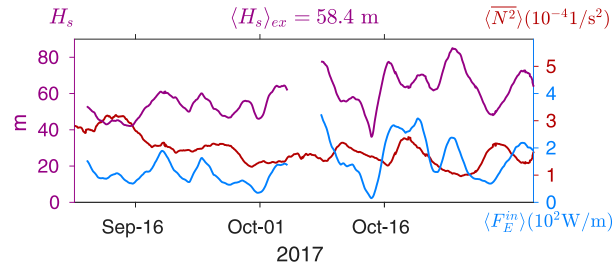

FIG. 5. Saturation depth H_s (purple; left axis), calculated on the basis of the mean baroclinic energy flux $\langle F_E^{\text{in}} \rangle$ (blue; right axis), and the mean stratification in the upper 40 m $\langle \overline{N^2} \rangle$ (red; right axis) at MS100. The data gap in $\langle F_E^{\text{in}} \rangle$ and thus H_s in the middle of the record is caused by a recovery and redeployment of the corresponding ADCP. The experiment-long average of the saturation depth is $\langle H_s \rangle_{\text{ex}} = 58.4$ m.

g. Validation

To validate the parameterization (7)–(11), we use all available energy ($\langle \text{APE} \rangle$), flux ($\langle F_E \rangle$) and dissipation ($\langle D \rangle$) measurements from every mooring deployed deeper than 20 m during the Inner Shelf Dynamics Experiment (ISDE). Since the parameterization is intended to predict mean quantities rather than instantaneous values, we compare $\langle \text{APE} \rangle$, $\langle F_E \rangle$, and $\langle D \rangle$ with APE^{par}, F_E^{par}, and $\partial_x F_E^{\text{par}}$, respectively (purple dots in Fig. 6). As input for the parameterization, we use $\langle \overline{N^2} \rangle$.

For both $\langle \text{APE} \rangle$ and $\langle F_E \rangle$, most of the 36-h windows are close to the one-to-one line (purple dots; black line in Figs. 6a, b), indicating a good agreement between parameterization and in situ observations over several orders of magnitude. At the smallest values of $\langle \text{APE} \rangle$ and $\langle F_E \rangle$, there is a slight overprediction, possibly associated with times when internal tide energy is simply too small to reach saturation. The cloud of points in Figs. 6a–c at large values corresponds to measurements made at mooring MS100, which lies outside the SR all of the time. Excluding MS100 (gray dots Fig. 6), the correlation between parameterized values and in situ observations, as based on the two month averages, is $r = 0.82$ for $\langle \text{APE} \rangle_{\text{ex}}$ and $r = 0.92$ for $\langle F_E \rangle_{\text{ex}}$.

The proposed parameterization applies only within the saturated range. This is clear in the nondimensionalized depiction of Figs. 6d–f. Outside the SR ($H_s/H < 1$), the parameterization strongly overpredicts, but as $H \rightarrow H_s$ the ratios $\text{APE}^{\text{par}}/\langle \text{APE} \rangle$ and $F_E^{\text{par}}/\langle F_E \rangle$ approach 1 (Figs. 6d, e), and these ratios scatter about 1 within the SR.

We have compared $\partial_x F_E^{\text{par}}$ with $\langle D \rangle$ and find them be highly correlated but find that $\partial_x F_E^{\text{par}}$ is larger than the in situ measurements ($\langle D \rangle$) by a factor of 2–3 in the SR (Figs. 6c, f). Either we have not sufficiently measured $\langle D \rangle$ or a significant fraction of $\partial_x F_E^{\text{par}}$ goes to processes other than turbulence. Our moored dissipation measurements do not include data from above 12 m, which means that we potentially miss a substantial part of the actual depth-integrated dissipation. At the same time, however, this also helps to reduce the effects of surface-forced turbulence helping to isolate the flux divergence-forced turbulence. One aspect that we have not investigated (and will in a separate study) is the possibility that the incoming tidal energy flux

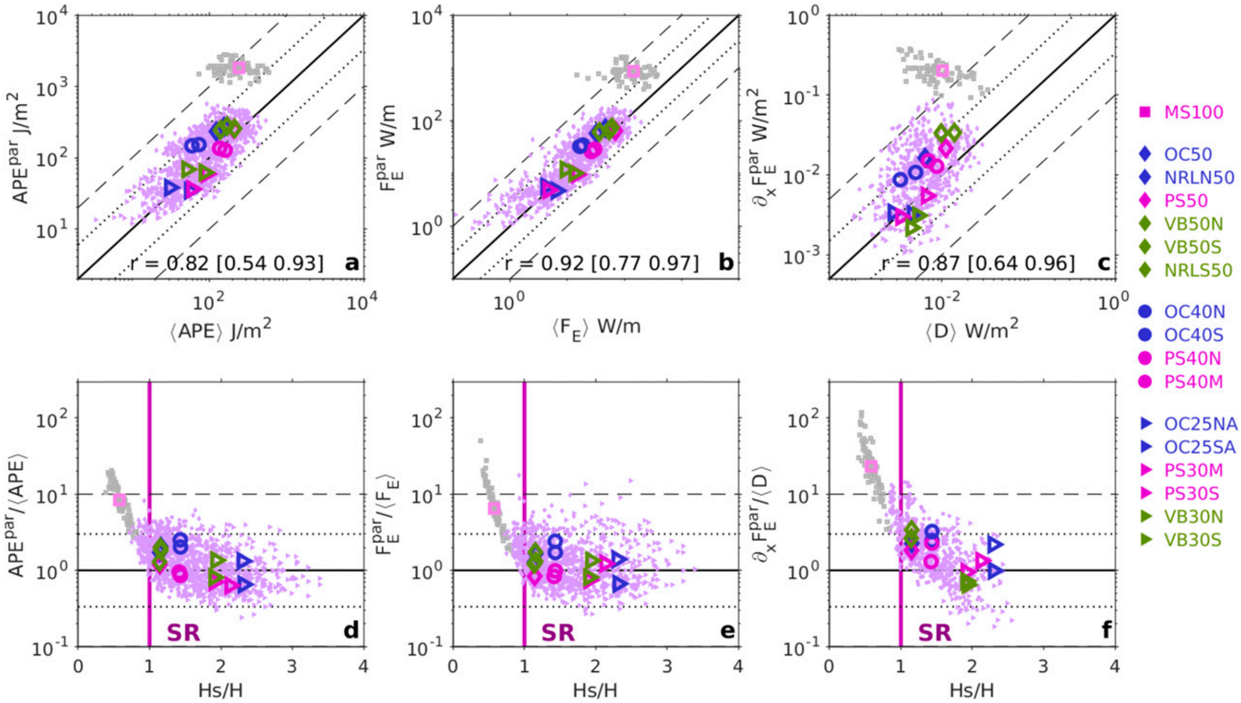

FIG. 6. Validation of parameterization (7)–(11). Shown is a comparison of (a) available potential energy, (b) baroclinic flux, and (c) depth-integrated dissipation rate between in situ measurements (x axis) and parameterized values (y axis). The correlation coefficients r at the bottom of (a)–(c) correspond to the colored symbols ($\langle\rangle_{\rm ex}$), excluding MS100 (pink square), where values in the square brackets are error bounds on r. The solid black lines in (a)–(f) indicate a one-to-one relation, dotted lines indicate a factor-of-three difference, and dashed lines indicate a factor-of-10 difference. Also shown is (d)–(f) a nondimensional comparison. The y axis is the ratio between parameterization and in situ observations, where values > 1 or < 1 indicate an over- or underprediction, respectively. The x axis is the saturation water depth H_s nondimensionalized by the respective mooring water depth H such that values > 1 or < 1 respectively lie inside or outside the saturated range. The vertical pink line indicates the edge between the saturated range and unsaturated range. Purple and gray dots are 36-h averages ($\langle\rangle$), and colored symbols are averages over the entire deployment period ($\langle\rangle_{\rm ex}$).

contributes to an internal wave setup (Umeyama and Shintani 2006), similar to surface wave setup on the beach. In this case, we would expect to see an increase in cross-shelf pressure gradient (which is well measured by high-resolution pressure sensors on many of the seafloor landers) and potentially an inertial response to that pressure gradient in the form of a northward-flowing current.

In general we find that, despite its simplicity, the parameterization (7)–(11) reproduces our in situ observations of energy and energy flux surprisingly well, producing a highly correlated though overestimated representation of dissipation (within a factor of 2–3) inside the saturated range.

3. Application of $F_E^{\rm par}$ and $\partial_x F_E^{\rm par}$ to the experimental site

We envision several useful application of the parameterization (7)–(11). It might be used, for instance, to generate maps of energy flux and dissipation over the inner shelf. To this end, we first calculate the gradient of the bathymetry of the entire region in which the ISDE has been conducted (Fig. 7a) to get H and $\partial_x H$. In a second step we interpolate the depth mean stratification between mooring locations (Fig. 7b) to get $\langle\overline{N^2}\rangle_{\rm ex}$ (Fig. 7b), where $\langle\rangle_{\rm ex}$ denotes an experiment-long averages. There are a number of different ways to obtain $\langle\overline{N^2}\rangle_{\rm ex}$. Here we assume that stratification measured at MS100 is representative for $\langle\overline{N^2}\rangle_{\rm ex}$ along the 100 m isobath to interpolate along isobaths between different moorings and in the last step in across-shore direction to get a regional coverage of $\langle\overline{N^2}\rangle_{\rm ex}$. Depending on the available data it is also possible to make different assumptions; for instance, if only one mooring is available one might assume horizontally uniform stratification. For the dataset presented here this is a reasonable assumption, with depth-mean stratification changing across the shelf by less than a factor of 2 (Fig. 7b). Either way, once H, $\partial_x H$, and $\langle\overline{N^2}\rangle_{\rm ex}$ are determined we can use (10) and (11) to calculated $F_E^{\rm par}$ and $\partial_x F_E^{\rm par}$ across the shelf (Figs. 7c, d).

A comparison between in situ observations (circles) and parameterized values suggests considerable similarity in the alongshore variability inside the SR (inshore of the white line marking $\langle H_s\rangle_{\rm ex}$ in Figs. 7c, d). Besides the general trend of decreasing flux, flux divergence and dissipation toward shore there can be identified some interesting local variability. In a region just north of Point Sal with steeper bathymetry ($\partial_x H \approx 7 \times 10^{-3}$) we find enhanced dissipation between 40- and 50-m water depth relative to other places along the

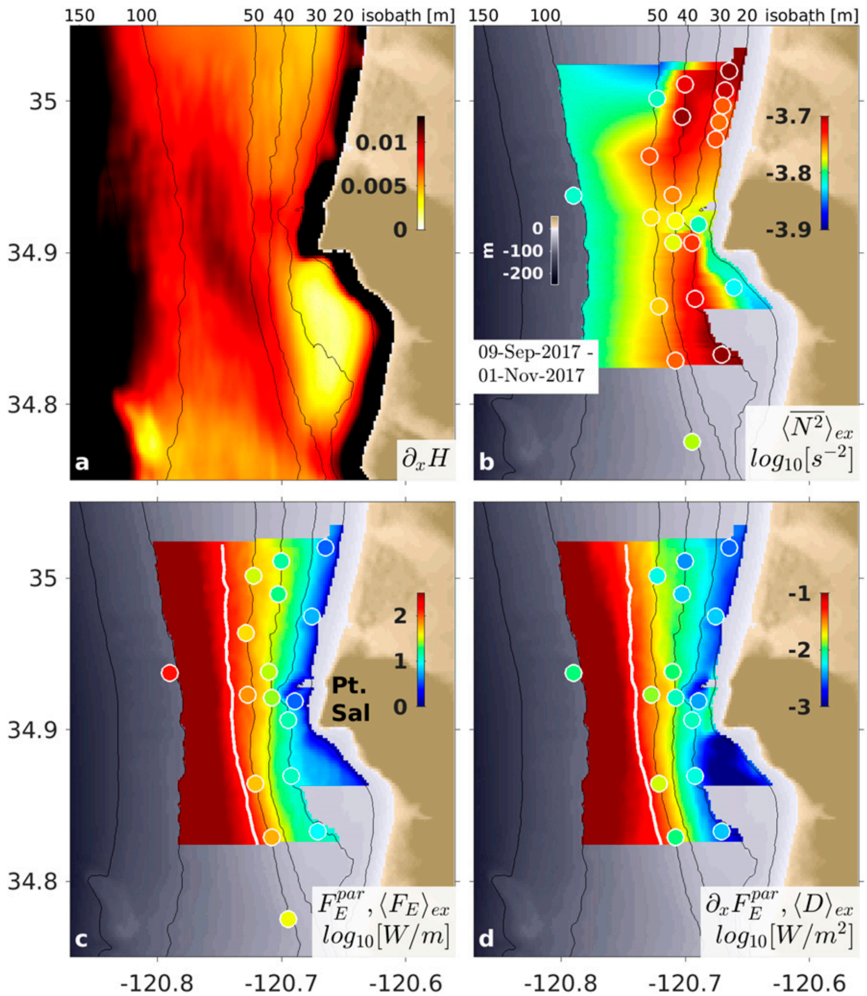

FIG. 7. Map of parameterized flux and flux divergence in comparison with in situ measurements of flux and dissipation: (a) bottom slope $\partial_x H$, (b) interpolation of depth averaged stratification $\langle \overline{N^2} \rangle_{\rm ex}$, (c) baroclinic energy flux $F_E^{\rm par}$, and (d) depth-integrated dissipation rate $\partial_x F_E^{\rm par}$. The colored circles in each panel show corresponding in situ observations at each mooring location. The white line in (c) and (d) illustrates the saturation depth $\langle H_s \rangle_{\rm ex}$, as based on (15). The maps correspond to average values ($\langle \rangle_{\rm ex}$) over the entire deployment length from 9 Sep to 1 Nov 2017.

same isobaths with smaller slopes (($\partial_x H \approx 5 \times 10^{-3}$ at OC and VB array). More dissipation can potentially yield more vertical mixing, which might be an explanation why $\langle \overline{N^2} \rangle_{\rm ex}$ is smaller directly off Point Sal relative to other regions farther north or south (Fig. 7b). Alternatively, this could be the result of headland related mixing processes, which are further investigated in Kovatch et al. (2021).

Inshore of $H = 30$ m, however, the slope just north of Point Sal becomes shallower, which results in a localized region of decreased dissipation, consistent in both parameterization and observation (small blue region in Fig. 7d). Similarly, south of Point Sal we find an extended region of small dissipation [$\partial_x F_E^{\rm par} = O(10^{-3})$ W m^{-2}] associated with a relatively shallow slope (($\partial_x H \approx 2 \times 10^{-3}$; cf. the yellow region in Fig. 7a and blue region in Fig. 7d south of Point Sal).

This demonstrates that the parameterization can predict, in addition to general cross-shore variations, some aspects of alongshore variability in $\langle F_E \rangle_{\rm ex}$ and $\langle D \rangle_{\rm ex}$ that are due to variations in bathymetry and stratification.

4. General applicability

In the following we test if the parameterization (7)–(11) is applicable beyond the dataset obtained during the ISDE. To this end we employ representative studies that list energy, energy flux or dissipation measurements on continental shelves at a range of worldwide locations. We then compare the direct measurements from these experiments with estimates that are based on our parameterization (7)–(11). As input for these calculations, we need bathymetry and stratification. Where not directly provided we make best guesses of $\langle\overline{N^2}\rangle$ and H as well as $\langle E\rangle$, $\langle F_E\rangle$, and $\langle D\rangle$ based on figures and tables from the respective publications and list these together with our corresponding parameterized values in Table 2. These studies cover a broad range of parameter space in terms of incoming internal tide energy and stratification (Fig. 8).

Colosi et al. (2018) present data from a pilot study to the ISDE described here, conducted close to our Point Sal array (see purple symbols in Fig. 1 in Part I) from mid-June to end of July 2015. Their energy flux measurements are well represented by (10) (see Table 2). Furthermore, the theory behind our parameterization is able to explain the finding of Colosi et al. (2018) that F_E is correlated to N^2 but not to the neap–spring cycle (see sections 5b and 5c). Based on an onshore decrease of $\langle F_E\rangle$, Colosi et al. (2018) calculate a dissipation length scale of roughly $L_D \approx 2$ km for both internal bores and high-frequency internal solitary waves. Our framework reproduces this result, with the surprising finding that L_D depends on bathymetry only (see section 5f).

Duda and Rainville (2008) describe data from four moorings deployed in the South China Sea during spring 2001. They find $\langle F_E\rangle$ to be dominated by diurnal frequencies. A comparison of $\langle F_E\rangle$ with $F_E^{\rm par}$ shows good agreement for the two shallower (85 and 120 m) moorings (Table 2). Using measured $\langle F_E\rangle$ values from the deeper (200 and 350 m) two moorings as input for (15) both predict saturation to be reached at $H_s \approx 140$ m.

This seems to be consistent with average dissipation data obtained by nearby microstructure measurements in spring 2005 (St. Laurent 2008), where average values of $\langle D\rangle$ are remarkably close to our prediction $\partial_x F_E^{\rm par}$ for water depths of $H = 50$–110 m. For $H > 190$ m, $\partial_x F_E^{\rm par}$ strongly overpredicts $\langle D\rangle$, which implies that $110 < H_s < 190$ m. Maximum dissipation is apparently reached near H_s (section 5e).

Shroyer et al. (2010a) describe data from the relatively shallow slope of the New Jersey shelf. They average three moorings (62, 72, and 82 m) together to provide a time series of daily averaged internal tidal energy (see Fig. 5 in Shroyer et al. 2010a). We average this time series in three consecutive periods (1–9 August, 9–15 August, and 15–25 August) for which average stratification data are available from Shroyer et al. (2010b). Using average wave speed estimates for these three periods [$c = 0.8$, 0.6, and 0.7 from Shroyer et al. (2011)], we are able to estimate $\langle F_E\rangle = c_g\langle E\rangle$. A comparison of $\langle F_E\rangle$ values from Shroyer et al. (2010a) with $F_E^{\rm par}$ estimates implies that during the first two periods the moorings lie just outside the saturated range ($H_s \approx 60$), whereas in the last higher energy period the moorings lie well within the saturated range.

Also, dissipation rates estimated by Shroyer et al. (2010a) based on shelfwide decay rates agree to within a factor of two with $\partial_x F_E^{\rm par}$ during the last two periods (Table 2). Shroyer et al. (2010a) developed a simple parameterization of dissipation based on the maximum energy, $\langle D\rangle = \mu E^{\max}$. We can use our parameterization (7) and (11) to develop a direct formula for the regression slope:

$$\mu = \frac{\langle\mathrm{APE}\rangle}{\mathrm{APE}^{\max}}\frac{\partial_x F_E^{\rm par}}{\mathrm{APE}^{\rm par}} = 4C_F\frac{\langle\mathrm{APE}\rangle}{\mathrm{APE}^{\max}}\langle\overline{N^2}\rangle^{1/2}\partial_x H. \tag{16}$$

Using the parameters from Table 1 and the stratification and bottom slope values provided in Shroyer et al. (2010a), (16) gives $\mu = 26.7$–$29.2 \times 10^{-6}\,\mathrm{s}^{-1}$, which is close to the value $\mu = 24 \times 10^{-6}\,\mathrm{s}^{-1}$ found by Shroyer et al. (2010a) using linear data fit.

Sharples et al. (2001) calculate total internal tidal energy and flux at two moorings in relatively deep water (110 and 150 m) with a relatively weak mean stratification on the New Zealand shelf. Agreement of $\langle F_E\rangle$ and $F_E^{\rm par}$ to within a factor of ~2 for both sites suggests that despite their depth both sites are inside the saturated regime where our parameterization is applicable. A similar agreement is found between $\partial_x\langle F_E\rangle$ and $\partial_x F_E^{\rm par}$ (Table 2).

A comparison with data provided by Holloway et al. (2001) over the Australian shelf show mixed agreement with our parameterization. We can use flux estimates from the deeper station to predict a saturation depth of roughly $H_s = 105$–120 m. Consistent with this we find that the ratio $F_E^{\rm par}/\langle F_E\rangle$ is within a factor of 4 inshore of $H = 125$ m (ignoring the station at 70 m). The big spread in $F_E^{\rm par}/\langle F_E\rangle$ at different stations can potentially be explained by the type of dataset. Holloway et al. (2001) provide data from three mooring stations (label m) with very sparse vertical resolution and no density measurement closer than 20 m to the surface and several full depth shipboard CTD stations (label c), which have been occupied for about 12 h each. The internal tide is therefore potentially underresolved either in time or space depending on the type of station, which might explain some of the mixed agreement to our parameterization.

A different type of dataset comes from Moum et al. (2007a) where single high-frequency solitons were tracked as they shoaled over the Oregon shelf. The ratio $F_E^{\rm par}/\langle F_E\rangle < 1.5$ inshore of $H = 122$ m and larger offshore, suggesting a saturated regime inshore from this point. Consistent with previous considerations we find maximum dissipation in the data to occur close to the saturation depth of $H_s \approx 120$ m. However, the predicted dissipation levels are larger than the measurements by between a factor of 2 and 20, which might suggest that high-frequency solitons are less dissipative than low-frequency internal tidal bores.

Other studies like MacKinnon and Gregg (2003b) from the New England shelf or Sherwin (1988) from the Malin shelf describe internal tides in places that appear to be outside the saturated range ($H > H_s$). This is indicated by a strong overprediction of our parameterization relative to the measured energy and dissipation levels of the internal tides.

In general, our parameterization seems to apply to other datasets with very different bottom slopes, stratification and over a range of energy levels, so long as the data lie within the saturated range. This is surprising given that we did not fine tune any of the free parameters but simply applied the parameters found during the ISDE (Table 1). Furthermore, it appears that we can apply this parameterization to waves of different frequencies from low-frequency diurnal tides (Duda and Rainville 2008) to high-frequency solitons

TABLE 2. Comparison between different observational studies and parameterized values from the saturation framework. The input parameters H, $\partial_x H$, and $\langle \overline{N^2} \rangle$ as well as the energy estimates $\langle E \rangle$, $\langle F_E \rangle$, and $\langle D \rangle$ are either directly given or are guessed on the basis of figure and tables of the respective studies. The parameterized values $\mathrm{APE}^{\mathrm{par}}$, F_E^{par}, and $\partial_x F_E^{\mathrm{par}}$ are calculated from (7), (10), and (11) with the given input parameters. The saturation depth H_s is either calculated by (15) with the corresponding $\langle F_E \rangle$ as $\langle F_E^{\mathrm{in}} \rangle$ or, where not feasible, as a guess on the basis of the ratio $F_E^{\mathrm{par}}/\langle F_E \rangle$.

Study and region	Observation						Parameterization				
	H (m)	$\partial_x H$ (10^{-3})	$\langle \overline{N^2} \rangle$ (10^{-4} s^{-2})	$\langle E \rangle$ ($\langle \mathrm{APE} \rangle$) (J m^{-2})	$\langle F_E \rangle$ (W m^{-1})	$\langle D \rangle$ (10^{-3} W m^{-2})	$\mathrm{APE}^{\mathrm{par}}$ (J m^{-2})	F_E^{par} (W m^{-1})	$\partial_x F_E^{\mathrm{par}}$ (10^{-3} W m^{-2})	H_s (m)	ratio $F_E^{\mathrm{par}}/\langle F_E \rangle$ ($\partial_x F_E^{\mathrm{par}}/\langle D \rangle$)
Colosi et al. (2018); Point Sal, CA	20	7	2.0	—	2–4	—	19	2.1	2.9		0.5–1.1
	30	7	2.0	—	12–18	—	65	10.5	9.8		0.6–0.9
	40	7	1.7	—	22–32	—	130	26	18		0.8–1.2
	50	7	0.5	—	8–13	—	75	10	5.7		0.8–1.3
	50	7	1.5	—	45–68	—	225	52	29		0.9–1.3
	50	7	2.0	—	80–100	—	299	81	45	>50	0.8–1.0
Duda and Rainville (2008); South China Sea	85	2.0	1.6	1090 (311)	440	—	1200	500	47		1.14
	120	3.3	1.5	3510 (560)	1510	—	3600	1700	180		1.13
	200	33	1.3	3620 (1220)	2120	—	12 100	10 400	6960	≈140	4.9
	350	4.4	0.9	2950 (740)	1660	—	44 600	55 600	2770		33
St. Laurent (2008); South China Sea	50	3	1.3	—	—	7	194	42	8		(1.14)
	75	2	1.3	—	—	16	660	210	20		(1.25)
	85	3	1.2	—	—	50	880	310	37		(0.74)
	110	3	1.0	—	—	65	1590	670	61	>110	(0.94)
	190	8	0.8	—	—	67	6560	4260	740	<190	(11)
	275	6	0.8	—	—	18	19 900	18 700	1560		(87)
Shroyer et al. (2010a); New Jersey shelf	72	0.1	4.58	724	580	20	2040	1200	67	60	2.08
	72	0.1	5.02	1540	925	61	2240	1380	77	65	1.50
	72	0.1	5.47	2730	1910	120	2440	1570	87	>72	0.82
Sharples et al. (2001); New Zealand shelf	110	2	0.6	480	192	—	955	311	23		1.6
		2	0.6	—	—	15	—	—	(38)		(2.5)
	150	2	0.6	1100	440	—	2420	1070	57	>150	2.4
Holloway et al. (2001); Australian North West shelf	65 (m)	1.8	1.95	31	0	0.7	640	222	25.2	0	—
	65 (c)	0.6	1.95	—	52	—	640	222	8.2	45	4.2
	70 (c)	1.3	1.91	—	20	—	780	288	21	35	14.4
	86 (c)	2.8	1.80	—	460	—	1360	600	79	80	1.3
	116 (c)	2.4	1.67	—	460	—	3120	1780	146	83	3.8
	124 (c)	0.9	1.65	—	1250	—	3750	2280	65	106	1.8
	125 (m)	3.0	1.64	1690	555	37.8	3800	2350	222	87	4.2
	132 (c)	1.9	1.63	—	1800	—	4470	2875	165	117	1.6
	162 (c)	3.0	1.57	—	1230	—	7980	6180	458	108	5.0
	300 (m)	7.8	1.45	1910	1080	42.7	47000	64900	6760	108	60

TABLE 2. (*Continued*)

Study and region	H (m)	$\partial_x H$ (10^{-3})	$\langle \overline{N^2} \rangle$ (10^{-4} s^{-2})	Observation: $\langle E \rangle$ ($\langle \mathrm{APE} \rangle$) (J m^{-2})	Observation: $\langle F_E \rangle$ (W m^{-1})	Observation: $\langle D \rangle$ (10^{-3} W m^{-2})	Parameterization: APE$^{\mathrm{par}}$ (J m^{-2})	Parameterization: F_E^{par} (W m^{-1})	Parameterization: $\partial_x F_E^{\mathrm{par}}$ (10^{-3} W m^{-2})	Parameterization: H_s (m)	Parameterization: ratio $F_E^{\mathrm{par}}/\langle F_E \rangle$ ($\partial_x F_E^{\mathrm{par}}/\langle D \rangle$)
				High-frequency solitons							
Moum et al. (2007a); Oregon shelf	70	3.0	3.28	1260	950	15	1350	650	112	77	0.69
	85	3.3	2.70	1460	1100	12	1980	1060	166	86	0.97
	95	4.0	2.42	1690	1270	10	2480	1400	236	93	1.11
	115	3.9	2.00	2380	1780	32	3630	2260	303	108	1.27
	122	3.8	1.88	2410	1810	150	4090	2610	323	111	1.45
	150	3.1	1.53	2380	1780	18	6180	4380	364	120	2.46
	150	2.1	1.53	2480	1860	6	6180	4380	241	121	2.36
	170	2.5	1.35	2840	2130	6	7940	5990	352	131	2.81
				Unsaturated							
MacKinnon and Gregg (2003b); New England shelf	70	2.5	4	—	130	(0.4–3.5)[a]	1640	880	125	≈45	6.8
Sherwin (1988); Malin shelf (Ireland)	165	1	1	280	60	0.7	5400	3400	82	≈75	>20
	190	1	1	580	104	1.3	8000	6000	125		>20

[a] The dissipation data for MacKinnon and Gregg (2003b) are based on depth- and time-averaged dissipation rates 5×10^{-9}–50×10^{-9} W kg^{-1} (MacKinnon and Gregg 2003a).

(Moum et al. 2007a). Since we make no assumptions about frequency in the derivation of (7)–(11), it is possible that this framework might be used for other shoaling internal waves with amplitudes large enough to be restricted by the water depth.

It is interesting to note that, where F_E^{par} agrees well with $\langle F_E \rangle$, APE$^{\mathrm{par}}$ is close to the measured total energy $\langle E \rangle$ and is greater than the APE fraction [see Duda and Rainville (2008), Sharples et al. (2001), Moum et al. (2007a), and Shroyer et al. (2010a) in Table 2]. This suggests a slightly different parameter combination at those studies with a smaller C_A and a larger C_F than what is observed here (Table 1). It is not surprising, however, that $\langle E \rangle$ follows a similar relation as APE$^{\mathrm{par}}$, since, analogous to $\langle \mathrm{APE} \rangle$, we expect $\langle \mathrm{KE} \rangle \propto \langle \overline{N^2} \rangle H^3$ (see the appendix).

5. Discussion

a. *Internal surf zone*

To our knowledge, the scaling outlined in section 2d to assess the evolution of the energetics of shoaling internal waves over the inner shelf is novel. However, analog scalings describe surf-zone dynamics (Thornton and Guza 1983; Sallenger and Holman 1985; Battjes 1988; Feddersen and Trowbridge 2005). Similar to our approach, it is assumed that breaking waves in the surf zone are saturated (Sallenger and Holman 1985; Battjes 1988) or self-similar (Feddersen and Trowbridge 2005), and the wave height (H_{rms}) is modeled as a constant fraction γ of the water depth, $H_{\mathrm{rms}} = \gamma H$. In the framework described in section 2 we look at saturation from an energetic point of view with the characteristic ratio APE$^{\max}$/APE$_c$, which corresponds to γ^2 in surf-zone dynamics given that the energy $E \propto H_{\mathrm{rms}}^2$.

Scaling equations for energy, energy flux, and dissipation in the surf zone analogous to those in section 2d have been described in the literature (Thornton and Guza 1983; Stive 1984; Battjes 1988; Feddersen and Trowbridge 2005; Feddersen 2012). Vertical stratification is the major additional complication that comes with internal waves when compared with surface waves. However, if we express stratification in terms of reduced gravity $g' = H\langle \overline{N^2} \rangle$, Eqs. (7), (10), and (11) can be formulated in a way that is equivalent to the surf-zone scalings (Table 3 presents a comparison). Note that despite very different scales in terms of wave speed, amplitude, period, and wavelength, the nondimensional parameter ξ is comparable between surface waves in the surf zone and internal waves on the inner shelf (Table 3).

The term *internal surf zone* has been used in the literature before, but in different contexts. The first example comes from the nature of internal waves propagating at angles critical to the local bottom slope. The group velocity of internal waves in a continuously stratified medium has a characteristic angle to the horizontal plane β that depends on the wave frequency and stratification. Eriksen (1985) pointed out the importance of locations on the continental slope where the bottom slope α_s is critical with respect to the group velocity angle of internal waves, $\beta \approx \alpha_s$. It was found that regions with critical slopes are often associated with elevated turbulence and mixing levels near the bottom (Ivey and Nokes 1989; Moum et al. 2002; Nash et al. 2004). This critical slope region was termed an *internal*

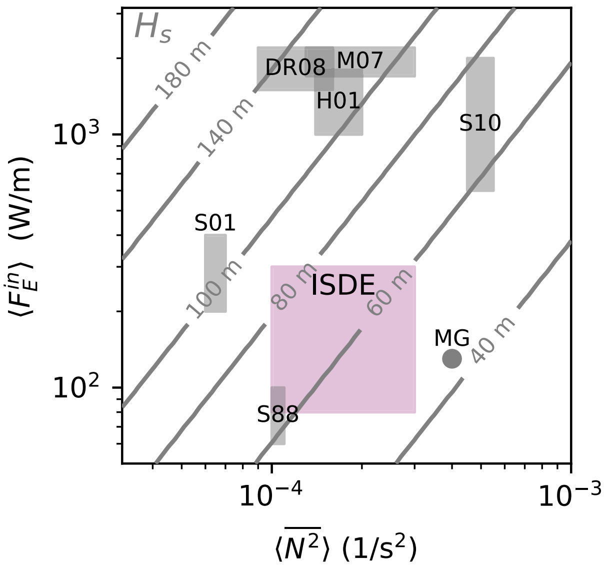

FIG. 8. Parameter space. Contour lines show H_s according to (15). The boxes represent different studies around the world: ISDE off the coast of California is described in this paper, S01 (Sharples et al. 2001) on the New Zealand shelf, S88 (Sherwin 1988) on Marlin shelf, DR08 (Duda and Rainville 2008) in the South China Sea, H01 (Holloway et al. 2001) on the Australian shelf, M07 (Moum et al. 2007a) on the Oregon shelf, S10 (Shroyer et al. 2010a) on the New Jersey shelf, and MG (MacKinnon and Gregg 2003b) on the New England shelf. The $\langle F_E^{\text{in}} \rangle$ represent long-term averages of the incoming baroclinic energy flux for all studies except for Moum et al. (2007a), where it corresponds to a short-term average over a single wave train. Note that the value of $\langle F_E^{\text{in}} \rangle$ from Sharples et al. (2001) is likely underestimated, since their deepest flux measurements was taken already inside the saturated range.

surf zone by Thorpe (1997). This definition has little to do with our definition since it could potentially refer to relatively deep sections of the continental shelf subject to different processes than the inner shelf.

More closely related to our definition, Bourgault and Kelley (2003) use the term *internal surf zone* to describe the shelf region beyond the breaking point of individual internal waves [see also Bourgault et al. (2008), where it is referred to as *internal beach*]. This break point is defined by the breaking water depth H_b (Vlasenko and Hutter 2002); H_b is calculated for individual waves by using an empirical formula by Vlasenko and Hutter (2002),

$$H_b = \frac{\eta_0}{\dfrac{0.8^\circ}{\alpha_s} + 0.4} + H_{\text{pyc}}, \tag{17}$$

with the slope angle in degrees, α_s, and the pycnocline depth H_{pyc}. In comparison, we identify the *internal surf zone* as a saturation range, defined as the region inshore of the saturation depth, H_s [see (15)]. The fact that these regimes are both defined by characteristic water depths is an interesting parallel. However, the critical distinction is that H_b refers to individual waves, H_s to the incident energy flux of the ensemble of waves associated with the internal tide. The H_s is determined by (15), a formula derived from simple energy considerations (see section 2). Using (17) for calculating H_b for typical waves found during the ISDE ($\alpha_s \approx 0.3^\circ$, $H_{\text{pyc}} = 15$ m, and a range of maximum isopycnal displacement $10 < \eta_0 < 40$ m) gives a range $18 < H_b < 28$ m, which is usually smaller than H_s. This indicates that direct breaking occurs closer to shore than first amplitude restriction by water depth, or in other words that our definition of the internal surf zone extends farther offshore than the definition of Bourgault and Kelley (2003). Our reference here to internal surf zone derives from the direct analogy of our scaling (see section 2) to commonly used surf-zone scalings (Thornton and Guza 1983; Sallenger and Holman 1985; see Table 3).

b. The internal tide loses its memory

An important finding from Part I is that the energy of the internal tide inshore of 40-m water depth is independent of the incoming energy flux $\langle F_E^{\text{in}} \rangle$ (see Fig. 9a in Part I). The concept of a saturated internal tide provides an explanation. From (10) we see that inside the SR the energy flux depends only on water depth and stratification and is independent of the incoming energy flux. Internal tide energy inside the SR is decoupled from the energy at the generation site. The internal tide loses memory of its initial strength during saturation.

At the same time, $\langle F_E^{\text{in}} \rangle$ influences H_s via (15). So although internal tide energy within the SR is independent of incoming energy levels, $\langle F_E^{\text{in}} \rangle$ determines the extent of the SR across the shelf.

c. Stratification channels energy onto the inner shelf

Another important finding from Part I is that, at the shallow moorings (<40 m), $\langle F_E \rangle$ is most strongly correlated to stratification (see Fig. 9b in Part I). The parameterization (10) implies that besides bathymetry $\langle F_E \rangle$ depends only on stratification inside the SR. This explains why we observe more energy close to shore during strong stratification periods than during weak stratification periods (see Fig. 7c in Part I).

Stratification also influences the extent of the SR across the shelf [(15)]. Stronger stratification leads to a smaller value of H_s and thus to a smaller cross-shore extent of the SR. On the other hand, when stratification is weak across the shelf, saturation occurs in deeper waters so that the internal tide loses its energy farther offshore.

Shelf stratification acts as a control that locates internal tide energy dissipation. Under strong stratification the energy is dissipated farther inshore and vice versa during periods of weak stratification.

d. Mixing feedback

Equation (11) implies that stronger stratification yields greater dissipation in the SR. A certain fraction of the dissipation goes to diapycnal mixing. Mixing causes $\langle N^2 \rangle$ to decrease, which via (11) causes dissipation/mixing to decrease, thus creating negative feedback. One potential consequence is a relatively constant background stratification over the inner shelf for extended periods. In this context one might ask how much of the internal tidal energy does contribute to diapycnal

TABLE 3. Analogy between inner shelf and surf zone. Reference key: TG83 (Thornton and Guza 1983), S84 (Stive 1984), B88 (Battjes 1988), FT05 (Feddersen and Trowbridge 2005), and F12 (Feddersen 2012).

	Surf zone (reference)	Inner shelf (reference)
	Geometry	
Depth range H	1–10 m	10–100 m
Horizontal extent	100–500 m	1–20 km
Bottom slope $\partial_x H$	0.02–0.06 (FT05)	0.001–0.01 (Table 2)
	Wave basics	
	Surface waves	Internal waves
Acceleration	$g = 9.81$ m s^{-2}	$g' = (\Delta\rho/\rho_0)g \propto H\langle\overline{N^2}\rangle$; $O(10^{-2})$ m s^{-2}
Wave speed	$c = (gH)^{1/2}$; $O(3–10)$ m s^{-1}	$c = \pi^{-1}\langle\overline{N^2}\rangle^{1/2}H \propto \sqrt{g'H}$; $O(0.1–0.5)$ m s^{-1} [(9)]
Amplitude	H_{rms}; $O(0.1–5)$ m (TG83)	η_0; $O(1–50)$ m
Period	$O(10)$ s	300–44 712 s
Wavelength λ	$O(30–100)$ m	$O(100–10\,000)$ m
Iribarren No. ξ	$\partial_x H\lambda^{1/2}H_{\mathrm{rms}}^{-1/2}$; $O(0.05–2)$	$\partial_x H\lambda^{1/2}\eta_0^{-1/2}$; $O(0.001–1)$
	Energy scaling	
Saturation level	$\gamma^2 = H_{\mathrm{rms}}^2/H^2$; $O(0.36–0.64)$ (B88) $O(0.1–0.8)$ (FT05)	$\mathrm{APE}^{\max}/\mathrm{APE}_c \propto C_A$ [(13)] $O(0.3)$ (Table 1)
Energy	$E = (1/8)\rho g H_{\mathrm{rms}}^2$ $E = (1/8)\gamma^2\rho g H^2$ (TG83) $O(10^4)$ J m^{-2}	$\mathrm{APE}^{\mathrm{par}} = (1/6)C_A\rho_0\langle\overline{N^2}\rangle H^3$ [(7)] $\mathrm{APE}^{\mathrm{par}} \propto C_A\rho_0 g' H^2$ $O(10^3)$ J m^{-2} (Table 2)
Energy flux	$F = (1/8)\rho g H_{\mathrm{rms}}^2 c$ $F = (1/8)\gamma^2\rho g^{3/2}H^{5/2}$ (S84) $O(10^3)$ W m^{-1}	$F_E^{\mathrm{par}} = (6\pi)^{-1}C_A C_F\rho_0\langle\overline{N^2}\rangle^{3/2}H^4$ [(10)] $F_E^{\mathrm{par}} \propto C_A C_F\rho_0 g'^{3/2}H^{5/2}$ $O(10^2)$ W m^{-1} (Table 2)
Dissipation	$D = \dfrac{5}{16}\gamma^2\rho g^{3/2}H^{3/2}\partial_x H$ (F12) $O(10^{-1})$ W m^{-2}	$\partial_x F_E^{\mathrm{par}} = [2C_{Fx}C_F/(3\pi)]C_A\rho_0\langle\overline{N^2}\rangle^{3/2}H^3\partial_x H$ [(11)] $\partial_x F_E^{\mathrm{par}} \propto C_A C_F\rho_0 g'^{3/2}H^{3/2}\partial_x H$ $O(10^{-2})$ W m^{-2} (Table 2)

mixing on the shelf? Given our observation that a major fraction of dissipation is happening in the well-mixed bottom region as opposed to the stratified interior, the overall mixing efficiency may be small. The feedback loop described above as well as the overall mixing efficiency of the internal tide on the inner shelf will be investigated in more detail in a following study.

e. *Cross-shelf structure of dissipation*

Equation (11) also indicates that, given moderate shelf slopes and cross-shelf changes in $\langle\overline{N^2}\rangle$, the tendency $\langle D\rangle \propto H^3$ ought to govern the cross-shelf structure in the SR. In addition, because internal tide propagation is not restricted by depth offshore of H_s, there ought to be a maximum in $\langle D\rangle$ near H_s.

The cross-shelf distribution of $\langle D\rangle$ normalized by its shelf-wide mean value shows a broad peak near and offshore of $H_s/H \approx 1$ (Fig. 9). This suggests that most internal tide dissipation on the shelf occurs as the internal tide begins to saturate. Therefore, (15) predicts the location of peak dissipation for a given incoming flux F_E^{in} and shelf stratification $\langle\overline{N^2}\rangle$. This cross-shelf distribution also roughly conforms to $\langle D\rangle \propto H^3$ (blue line in Fig. 9).

f. *Dissipation length scale*

From the ISDE pilot experiment in 2015, Colosi et al. (2018) estimated the length scale over which the internal tide dissipates its energy by fitting an exponential to $\langle F_E\rangle$ measured at moorings distributed across the inner shelf. These mooring locations roughly correspond to the Point Sal array shown here (magenta symbols in Fig. 1 in Part I). They find this *e*-folding length scale, which can be interpreted as a dissipation length scale for internal waves, to be relatively insensitive to environmental condition and/or frequency. Their estimates were based on independent evaluations of internal tidal bores and higher-frequency, large-amplitude wave packets and was 2.0–2.4 km in both cases.

From the framework developed in section 2 we derive an expression for the dissipation length scale by dividing (10) by (11),

$$L_D = \frac{F_E^{\mathrm{par}}}{\partial_x F_E^{\mathrm{par}}} \approx \frac{1}{4}\frac{H}{\partial_x H} \quad (\mathrm{m}). \tag{18}$$

That is, L_D depends only on the bathymetry. Approximating the bottom slope $\partial_x H \approx H/L_{\mathrm{shore}}$, where L_{shore} is simply distance to shore, $L_D \propto L_{\mathrm{shore}}$. The typical dissipation length scale is proportional to the distance to shore. From bathymetry data along the mooring locations used by Colosi et al. (2018) in (18) we find L_D =1.2–2.5 km, which corresponds to the *e*-folding scale found independently by Colosi et al. (2018) of 2.0–2.4 km. Since L_D is independent of wave frequency, (18) ought to apply to all large-amplitude shoaling internal waves and not just to the low-frequency internal tides.

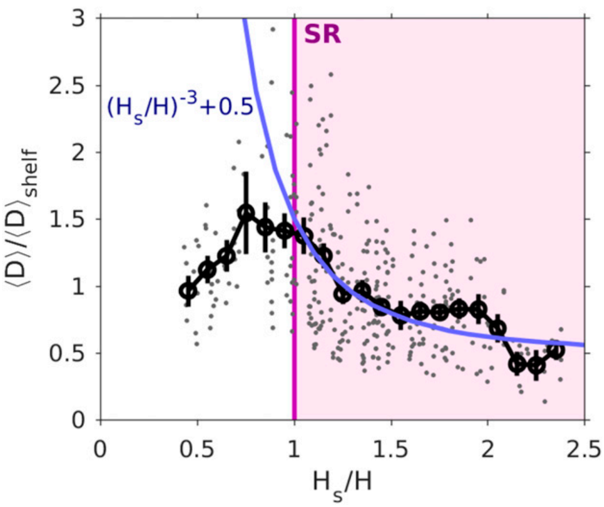

FIG. 9. Nondimensional cross-shelf distribution of energy dissipation. The gray dots show 36-h hour averages of depth-integrated dissipation $\langle D \rangle$ for each mooring, normalized by the respective shelfwide-averaged dissipation rate $\langle D \rangle_{\mathrm{shelf}}$, vs nondimensional water depth H_s/H; $H_s/H > 1$ represents the saturated inner shelf (shading). The black circles are bin averages with respective 95% bootstrap uncertainty (vertical black lines) The blue line corresponds to a $\langle D \rangle \propto H^3$ relation as suggested by (11) with an arbitrary background dissipation.

g. Limitations

Inside the SR, the predictions of (7)–(11) agree reasonably well with data, but $\langle D \rangle \propto H^3$ creates a large overprediction outside the SR. Hence a clear determination of H_s, which varies with time, is important.

Another limitation arises from the fact that we implicitly assume a cross-shore bathymetry profile with monotonically decreasing water depth toward shore. If we imagine more complex bathymetries with local regions of very shallow or even negative slope our parameterization yields nonphysical results. Equation (11), for instance, predicts negative dissipation rates where $\partial_x H < 0$. The problem is that in such regions the assumption of local saturation is not satisfied. Therefore, the parameterization likely fails to describe shelves, which are very wide; for example, the Northwest European shelf with mean slopes of $\partial_x H < 10^{-4}$. The saturation constraint imposed by the sloping bottom in these regions is probably only valid in localized places with steeper topography. Propagating over extended regions of flat bathymetry, internal waves will lose considerable and potentially all energy to bottom friction, which may result in an undersaturated state that cannot accurately be described by our parameterization.

Furthermore, it is important to note that the parameterization is only meant to predict the inner shelf dissipation due to shoaling internal waves. There are inner shelf regions in the world where other forcing mechanisms, including winds and barotropic tides, are more important than internal waves in terms of energy dissipation. But we expect that, at these locations, the parameterization can be used to estimate the internal tide's contribution to dissipation even if small relative to other sources. In this context it is worth noting that even on shelves where barotropic tidal currents are the dominant source for dissipation via turbulence, internal waves are important contributors to diapycnal mixing. Since barotropic tides dissipate most of their energy at the seafloor, they are likely associated with smaller bulk mixing efficiencies (Simpson and Hunter 1974) than internal waves (Stigebrandt and Aure 1989), which often generate shear instabilities in the pycnocline itself (Moum et al. 2003).

h. Variability of model parameters

An issue with the applicability of our parameterization (7)–(11) is the value of the free parameters C_A and C_F may change in different systems. Parameter C_F depends on wave reflectivity as well as the ratio between $\langle \mathrm{APE} \rangle$ and $\langle \mathrm{KE} \rangle$. The latter is known to change for freely propagating waves depending on frequency and latitude (see also section 2e). However, as we demonstrate in the appendix, the wave energy in the saturated range is simultaneously limited by APE_c and KE_c, which suggests that the ratio $\langle \mathrm{APE} \rangle / \langle \mathrm{KE} \rangle$ does not substantially change once a system is in a saturated state.

The reflection rate on the other hand will strongly depend on the steepness of the bottom slope. Bourgault and Kelley (2007) suggest that the reflection rate of individual waves can be parameterized with ξ. Using their parameterization for typical waves found during the ISDE (see Fig. 1) the reflection rates lies between 10% and 30%. This is in agreement with our considerations in section 2e in the context of Fig. 4. How and whether C_F depends on ξ and other possible parameters would be an interesting subject for further investigations. In general, we expect smaller C_F for steeper slopes. However, also highly nonlinear waves will have a tendency to radiate energy away from steep fronts in both direction, thus potentially causing a fraction of the energy to radiated against the propagation direction of the main wave.

Parameter C_A is composed of the maximum saturation $\mathrm{APE}^{\max}/\mathrm{APE}_c$ and the wave shape parameter $\langle \mathrm{APE} \rangle / \mathrm{APE}^{\max}$. It can be expected that the maximum saturation is not varying by much in different saturated systems. The wave shape, however, can potentially be very different. Here we observe very frequent strong internal tidal bores every 6–12 h. This means that we have a relatively strong isopycnal displacement from a potential rest state most of the time. The value of $\langle \mathrm{APE} \rangle / \mathrm{APE}^{\max} = 0.26$ measured here is therefore probably on the high end for long-term averages. If strong displacements occur, more intermittent $\langle \mathrm{APE} \rangle / \mathrm{APE}^{\max}$ is likely found to be smaller than here.

6. Summary and conclusions

From Part I we made several relevant observations about the averaged internal tides shoaling over the inner shelf of California:

1) the internal tide dissipates most of its energy between the 100- and 20-m isobaths;

2) approaching shallower water, the internal tide's energy flux becomes progressively decorrelated from the offshore incident wave's energy flux; and
3) internal tide stratification controls how much internal tide energy is tunneled to shallower sites such that
4) inshore energy levels of the internal tide are entirely independent of the incoming internal tide.

Importantly, we find that the internal tide loses memory of its initial strength as it shoals.

We consider these observations in terms of a conceptual framework in which the internal tide saturates as is shoals. Simply, the depth of the water column limits the amplitude η_0 of the internal tidal wave, both of which decrease toward shallow water. Since the tidal wave energy is proportional to η^2 [(4)], the internal tide loses energy as it propagates onshore. We show that the maximum capacity of the vertically integrated available potential energy (APE_c) of the internal tide depends on the depth-averaged stratification and H^3 [(5)]. For an internal wave to propagate shoreward past the point of saturation, where its energy is a certain fraction of the maximum capacity, it must lose energy at a rate dictated by the decreasing energy capacity of the water column. This concept of wave saturation in shallow waters is a well-known phenomenon for surface waves, where inside the surf zone the wave height is found to be a certain fraction of the water depth.

We then use the idea of a saturated internal tide to develop simple parameterizations for $\langle \mathrm{APE} \rangle$, $\langle F_E \rangle$, and $\partial_x \langle F_E \rangle$ (which we interpret as $\langle D \rangle$) inside the saturated range (7)–(11). The parameterization requires only the depth-mean background stratification and bathymetry, permitting application based on a minimal amount of information of the system. A test of the parameterization using the data from our experiment shows surprisingly good agreement within the saturated range.

The theoretical framework of the saturated internal tide makes additional points:

1) it explains the memory loss of the internal tide and the controlling role of stratification on internal tide energy on the shelf;
2) it predicts that peak dissipation rates on the shelf are found close to the location of the saturation depth H_s—a point confirmed by our measurements;
3) an expression is derived for the dissipation length scale of the internal tide inside the saturated range that depends only on bathymetry; and
4) an empirical parameterization of dissipation that is based on internal tide peak energies found by Shroyer et al. (2010a) is confirmed and is theoretically derived.

We applied our parameterization to a range of shelf sites with varying energies and stratifications where experiments with measurements of $\langle \mathrm{APE} \rangle$, $\langle F_E \rangle$, and/or dissipation have been undertaken (Table 2). The resultant predictions suggests that our parameterization is broadly applicable, including application to high-frequency solitary waves and lower-frequency diurnal tides, beyond that of semidiurnal internal tides examined in detail here.

The inner shelf has been previously defined in terms of its response to wind forcing (Lentz 1994; Fewings et al. 2008). The applicability of our parameterization at a range of sites suggests that a saturated range for the internal tide is an intrinsic feature of the inner shelf. This might yield a new or additional definition of the inner shelf from an internal tide perspective: *the inner shelf is that part of the continental shelf where the internal tide saturates.* The analogy of our framework to surface waves approaching the beach suggests that the inner shelf is the surf zone for the internal tide.

Acknowledgments. The work described here was fully funded by the Office of Naval Research through the Inner Shelf DRI. We are grateful to Falk Fedderson, Jim Thomson, and Matthew Spydell for pointing out the connection of our framework to surf-zone dynamics. We are grateful to two anonymous reviewers and editor Jody Klymak for their time and valuable comments.

Data availability statement. All data used in this paper are achieved and publicly available (https://doi.org/10.6075/J0WD3Z3Q).

APPENDIX

Kinetic Energy Capacity

Analogous to (5), it is possible to derive a maximum capacity for the kinetic energy of a given water column. The depth-integrated kinetic energy is

$$\mathrm{KE} = \frac{1}{2}\rho_0 \int_0^H u^2\, dz \quad (\mathrm{J\ m^{-2}}). \tag{A1}$$

We assume that the flow is subcritical on average ($\mathrm{Fr} = u/c_0 < 1$). Although this may not be the case for highly nonlinear waves where internal recirculation occurs, we expect it to be the typical case. We consider $u = c_0$ to be the upper bound in (A1), which yields an expression for the maximum capacity of kinetic energy,

$$\mathrm{KE}_c = \frac{1}{2}\rho_0 c_0^2 \int_0^H dz = \frac{1}{2\pi^2}\rho_0 \langle \overline{N^2} \rangle H^3, \tag{A2}$$

using (9).

Aside from the prefactor, (A2) is equivalent to (5). That is, the framework developed in section 2d could alternatively be based on KE_c rather than on APE_c. Since both KE_c and APE_c change simultaneously with energy restrictions on the shoaling internal waves we expect that the ratio $\langle \mathrm{APE} \rangle / \langle \mathrm{KE} \rangle$ does not change inside the saturated range.

REFERENCES

Aghsaee, P., L. Boegman, and K. G. Lamb, 2010: Breaking of shoaling internal solitary waves. *J. Fluid Mech.*, **659**, 289–317, https://doi.org/10.1017/S002211201000248X.

Alford, M., J. MacKinnon, Z. Zhao, R. Pinkel, J. Klymak, and T. Peacock, 2007: Internal waves across the pacific. *Geophys. Res. Lett.*, **34**, L24601, https://doi.org/10.1029/2007GL031566.

Arthur, R. S., and O. B. Fringer, 2014: The dynamics of breaking internal solitary waves on slopes. *J. Fluid Mech.*, **761**, 360–398, https://doi.org/10.1017/jfm.2014.641.

Barad, M. F., and O. B. Fringer, 2010: Simulations of shear instabilities in interfacial gravity waves. *J. Fluid Mech.*, **644**, 61–95, https://doi.org/10.1017/S0022112009992035.

Battjes, J., 1988: Surf-zone dynamics. *Annu. Rev. Fluid Mech.*, **20**, 257–291, https://doi.org/10.1146/annurev.fl.20.010188.001353.

Becherer, J., J. N. Moum, J. A. Colosi, J. A. Lerczak, and J. M. McSweeney, 2020: Turbulence asymmetries in bottom boundary layer velocity pulses associated with onshore-propagating nonlinear internal waves. *J. Phys. Oceanogr.*, **50**, 2373–2391, https://doi.org/10.1175/JPO-D-19-0178.1.

——, and Coauthors, 2021: Saturation of the internal tide over the inner continental shelf. Part I: Observations. *J. Phys. Oceanogr.*, **51**, 2553–2563, https://doi.org/10.1175/JPO-D-20-0264.1.

Boegman, L., and G. N. Ivey, 2009: Flow separation and resuspension beneath shoaling nonlinear internal waves. *J. Geophys. Res.*, **114**, C02018, https://doi.org/10.1029/2007JC004411.

——, and M. Stastna, 2019: Sediment resuspension and transport by internal solitary waves. *Annu. Rev. Fluid Mech.*, **51**, 129–154, https://doi.org/10.1146/annurev-fluid-122316-045049.

——, G. Ivey, and J. Imberger, 2005: The degeneration of internal waves in lakes with sloping topography. *Limnol. Oceanogr.*, **50**, 1620–1637, https://doi.org/10.4319/lo.2005.50.5.1620.

Bogucki, D. J., and C. Garrett, 1993: A simple model for the shear-induced decay of an internal solitary wave. *J. Phys. Oceanogr.*, **23**, 1767–1776, https://doi.org/10.1175/1520-0485(1993)023<1767:ASMFTS>2.0.CO;2.

——, and L. G. Redekopp, 1999: A mechanism for sediment resuspension by internal solitary waves. *Geophys. Res. Lett.*, **26**, 1317–1320, https://doi.org/10.1029/1999GL900234.

Bourgault, D., and D. E. Kelley, 2003: Wave-induced boundary mixing in a partially mixed estuary. *J. Mar. Res.*, **61**, 553–576, https://doi.org/10.1357/002224003771815954.

——, and ——, 2007: On the reflectance of uniform slopes for normally incident interfacial solitary waves. *J. Phys. Oceanogr.*, **37**, 1156–1162, https://doi.org/10.1175/JPO3059.1.

——, ——, and P. S. Galbraith, 2008: Turbulence and boluses on an internal beach. *J. Mar. Res.*, **66**, 563–588, https://doi.org/10.1357/002224008787536835.

Butman, B., P. Alexander, A. Scotti, R. Beardsley, and S. Anderson, 2006: Large internal waves in Massachusetts bay transport sediments offshore. *Cont. Shelf Res.*, **26**, 2029–2049, https://doi.org/10.1016/j.csr.2006.07.022.

Carr, M., P. A. Davies, and P. Shivaram, 2008: Experimental evidence of internal solitary wave-induced global instability in shallow water benthic boundary layers. *Phys. Fluids*, **20**, 066603, https://doi.org/10.1063/1.2931693.

Colosi, J. A., N. Kumar, S. H. Suanda, T. M. Freismuth, and J. H. MacMahan, 2018: Statistics of internal tide bores and internal solitary waves observed on the inner continental shelf off Point Sal, California. *J. Phys. Oceanogr.*, **48**, 123–143, https://doi.org/10.1175/JPO-D-17-0045.1.

Duda, T. F., and L. Rainville, 2008: Diurnal and semidiurnal internal tide energy flux at a continental slope in the South China sea. *J. Geophys. Res.*, **113**, C03025, https://doi.org/10.1029/2007JC004418.

Eriksen, C. C., 1985: Implications of ocean bottom reflection for internal wave spectra and mixing. *J. Phys. Oceanogr.*, **15**, 1145–1156, https://doi.org/10.1175/1520-0485(1985)015<1145:IOOBRF>2.0.CO;2.

Feddersen, F., 2012: Observations of the surf-zone turbulent dissipation rate. *J. Phys. Oceanogr.*, **42**, 386–399, https://doi.org/10.1175/JPO-D-11-082.1.

——, and J. Trowbridge, 2005: The effect of wave breaking on surf-zone turbulence and alongshore currents: A modeling study. *J. Phys. Oceanogr.*, **35**, 2187–2203, https://doi.org/10.1175/JPO2800.1.

Fewings, M., S. J. Lentz, and J. Fredericks, 2008: Observations of cross-shelf flow driven by cross-shelf winds on the inner continental shelf. *J. Phys. Oceanogr.*, **38**, 2358–2378, https://doi.org/10.1175/2008JPO3990.1.

Gough, M. K., T. M. Freismuth, J. H. MacMahan, J. A. Colosi, S. H. Suanda, and N. Kumar, 2020: Heating of the midshelf and inner shelf by warm internal tidal bores. *J. Phys. Oceanogr.*, **50**, 2609–2620, https://doi.org/10.1175/JPO-D-19-0143.1.

Grimshaw, R., E. Pelinovsky, T. Talipova, and A. Kurkin, 2004: Simulation of the transformation of internal solitary waves on oceanic shelves. *J. Phys. Oceanogr.*, **34**, 2774–2791, https://doi.org/10.1175/JPO2652.1.

Helfrich, K. R., and W. K. Melville, 2006: Long nonlinear internal waves. *Annu. Rev. Fluid Mech.*, **38**, 395–425, https://doi.org/10.1146/annurev.fluid.38.050304.092129.

Holloway, P. E., E. Pelinovsky, and T. Talipova, 1999: A generalized Korteweg-de Vries model of internal tide transformation in the coastal zone. *J. Geophys. Res.*, **104**, 18 333–18 350, https://doi.org/10.1029/1999JC900144.

——, P. G. Chatwin, and P. Craig, 2001: Internal tide observations from the Australian North West shelf in summer 1995. *J. Phys. Oceanogr.*, **31**, 1182–1199, https://doi.org/10.1175/1520-0485(2001)031<1182:ITOFTA>2.0.CO;2.

Inall, M. E., T. P. Rippeth, and T. J. Sherwin, 2000: Impact of nonlinear waves on the dissipation of internal tidal energy at a shelf break. *J. Geophys. Res.*, **105**, 8687–8705, https://doi.org/10.1029/1999JC900299.

Ivey, G., and R. Nokes, 1989: Vertical mixing due to the breaking of critical internal waves on sloping boundaries. *J. Fluid Mech.*, **204**, 479–500, https://doi.org/10.1017/S0022112089001849.

Kang, D., and O. Fringer, 2010: On the calculation of available potential energy in internal wave fields. *J. Phys. Oceanogr.*, **40**, 2539–2545, https://doi.org/10.1175/2010JPO4497.1.

——, and ——, 2012: Energetics of barotropic and baroclinic tides in the Monterey Bay Area. *J. Phys. Oceanogr.*, **42**, 272–290, https://doi.org/10.1175/JPO-D-11-039.1.

Klymak, J. M., and J. N. Moum, 2003: Internal solitary waves of elevation advancing on a shoaling shelf. *Geophys. Res. Lett.*, **30**, 2045, https://doi.org/10.1029/2003GL017706.

——, M. H. Alford, R. Pinkel, R.-C. Lien, Y. J. Yang, and T.-Y. Tang, 2011: The breaking and scattering of the internal tide on a continental slope. *J. Phys. Oceanogr.*, **41**, 926–945, https://doi.org/10.1175/2010JPO4500.1.

Kovatch, M., F. Feddersen, D. G. Grimes, and J. H. MacMahan, 2021: Vorticity recirculation and asymmetric generation at a small headland with broadband currents. *J. Geophys. Res. Oceans*, **126**, e2020JC016639, https://doi.org/10.1029/2020JC016639.

Kumar, N., S. Suanda, J. Colosi, K. Haas, E. DiLorenzo, A. Miller, and C. Edwards, 2019: Coastal semidiurnal internal tidal incoherence in the Santa Maria Basin, California: Observations and model simulations. *J. Geophys. Res. Oceans*, **124**, 5158–5179, https://doi.org/10.1029/2018JC014891.

——, and Coauthors, 2021: The Inner-Shelf Dynamics Experiment. *Bull. Amer. Meteor. Soc.*, **102**, E1033–E1063, https://doi.org/10.1175/BAMS-D-19-0281.1.

Lamb, K. G., 2014: Internal wave breaking and dissipation mechanisms on the continental slope/shelf. *Annu. Rev. Fluid Mech.*, **46**, 231–254, https://doi.org/10.1146/annurev-fluid-011212-140701.

——, and D. Farmer, 2011: Instabilities in an internal solitary-like wave on the oregon shelf. *J. Phys. Oceanogr.*, **41**, 67–87, https://doi.org/10.1175/2010JPO4308.1.

Lentz, S. J., 1994: Current dynamics over the northern California inner shelf. *J. Phys. Oceanogr.*, **24**, 2461–2478, https://doi.org/10.1175/1520-0485(1994)024<2461:CDOTNC>2.0.CO;2.

MacKinnon, J., and M. Gregg, 2003a: Mixing on the late-summer New England shelf—Solibores, shear, and stratification. *J. Phys. Oceanogr.*, **33**, 1476–1492, https://doi.org/10.1175/1520-0485(2003)033<1476:MOTLNE>2.0.CO;2.

——, and ——, 2003b: Shear and baroclinic energy flux on the summer New England shelf. *J. Phys. Oceanogr.*, **33**, 1462–1475, https://doi.org/10.1175/1520-0485(2003)033<1462:SABEFO>2.0.CO;2.

McSweeney, J. M., and Coauthors, 2020a: Alongshore variability of shoaling internal bores on the inner shelf. *J. Phys. Oceanogr.*, **50**, 1–50, https://doi.org/10.1175/JPO-D-20-0090.1.

——, and Coauthors, 2020b: Observations of shoaling nonlinear internal bores across the central California inner shelf. *J. Phys. Oceanogr.*, **50**, 111–132, https://doi.org/10.1175/JPO-D-19-0125.1.

Moum, J., D. Caldwell, J. Nash, and G. Gunderson, 2002: Observations of boundary mixing over the continental slope. *J. Phys. Oceanogr.*, **32**, 2113–2130, https://doi.org/10.1175/1520-0485(2002)032<2113:OOBMOT>2.0.CO;2.

——, D. Farmer, W. Smyth, L. Armi, and S. Vagle, 2003: Structure and generation of turbulence at interfaces strained by internal solitary waves propagating shoreward over the continental shelf. *J. Phys. Oceanogr.*, **33**, 2093–2112, https://doi.org/10.1175/1520-0485(2003)033<2093:SAGOTA>2.0.CO;2.

——, ——, E. Shroyer, W. Smyth, and L. Armi, 2007a: Dissipative losses in nonlinear internal waves propagating across the continental shelf. *J. Phys. Oceanogr.*, **37**, 1989–1995, https://doi.org/10.1175/JPO3091.1.

——, J. Klymak, J. Nash, A. Perlin, and W. Smyth, 2007b: Energy transport by nonlinear internal waves. *J. Phys. Oceanogr.*, **37**, 1968–1988, https://doi.org/10.1175/JPO3094.1.

Nash, J. D., E. Kunze, J. M. Toole, and R. W. Schmitt, 2004: Internal tide reflection and turbulent mixing on the continental slope. *J. Phys. Oceanogr.*, **34**, 1117–1134, https://doi.org/10.1175/1520-0485(2004)034<1117:ITRATM>2.0.CO;2.

——, M. H. Alford, and E. Kunze, 2005: Estimating internal wave energy fluxes in the ocean. *J. Atmos. Oceanic Technol.*, **22**, 1551–1570, https://doi.org/10.1175/JTECH1784.1.

——, S. M. Kelly, E. L. Shroyer, J. N. Moum, and T. F. Duda, 2012: The unpredictable nature of internal tides on continental shelves. *J. Phys. Oceanogr.*, **42**, 1981–2000, https://doi.org/10.1175/JPO-D-12-028.1.

Pomar, L., M. Morsilli, P. Hallock, and B. Bádenas, 2012: Internal waves, an under-explored source of turbulence events in the sedimentary record. *Earth-Sci. Rev.*, **111**, 56–81, https://doi.org/10.1016/j.earscirev.2011.12.005.

Rippeth, T. P., and M. E. Inall, 2002: Observations of the internal tide and associated mixing across the Malin shelf. *J. Geophys. Res.*, **107**, 3028, https://doi.org/10.1029/2000JC000761.

Sallenger, A. H., and R. A. Holman, 1985: Wave energy saturation on a natural beach of variable slope. *J. Geophys. Res.*, **90**, 11 939–11 944, https://doi.org/10.1029/JC090iC06p11939.

Sandstrom, H., and J. Elliott, 1984: Internal tide and solitons on the Scotian shelf: A nutrient pump at work. *J. Geophys. Res.*, **89**, 6415–6426, https://doi.org/10.1029/JC089iC04p06415.

——, and N. Oakey, 1995: Dissipation in internal tides and solitary waves. *J. Phys. Oceanogr.*, **25**, 604–614, https://doi.org/10.1175/1520-0485(1995)025<0604:DIITAS>2.0.CO;2.

Scotti, A., and J. Pineda, 2007: Plankton accumulation and transport in propagating nonlinear internal fronts. *J. Mar. Res.*, **65**, 117–145, https://doi.org/10.1357/002224007780388702.

——, R. C. Beardsley, B. Butman, and J. Pineda, 2008: Shoaling of nonlinear internal waves in Massachusetts Bay. *J. Geophys. Res.*, **113**, C08031, https://doi.org/10.1029/2008JC004726.

Sharples, J., C. M. Moore, and E. R. Abraham, 2001: Internal tide dissipation, mixing, and vertical nitrate flux at the shelf edge of NE New Zealand. *J. Geophys. Res.*, **106**, 14 069–14 081, https://doi.org/10.1029/2000JC000604.

——, and Coauthors, 2007: Spring-neap modulation of internal tide mixing and vertical nitrate fluxes at a shelf edge in summer. *Limnol. Oceanogr.*, **52**, 1735–1747, https://doi.org/10.4319/lo.2007.52.5.1735.

Sherwin, T., 1988: Analysis of an internal tide observed on the Malin shelf, north of Ireland. *J. Phys. Oceanogr.*, **18**, 1035–1050, https://doi.org/10.1175/1520-0485(1988)018<1035:AOAITO>2.0.CO;2.

Shroyer, E. L., J. Moum, and J. Nash, 2010a: Energy transformations and dissipation of nonlinear internal waves over New Jersey's continental shelf. *Nonlinear Processes Geophys.*, **17**, 345–360, https://doi.org/10.5194/npg-17-345-2010.

——, J. N. Moum, and J. D. Nash, 2010b: Vertical heat flux and lateral mass transport in nonlinear internal waves. *Geophys. Res. Lett.*, **37**, L08601, https://doi.org/10.1029/2010GL042715.

——, ——, and ——, 2011: Nonlinear internal waves over new jersey's continental shelf. *J. Geophys. Res.*, **116**, C03022, https://doi.org/10.1029/2010JC006332.

Simpson, J., and J. Hunter, 1974: Fronts in the Irish sea. *Nature*, **250**, 404–406, https://doi.org/10.1038/250404a0.

St. Laurent, L., 2008: Turbulent dissipation on the margins of the South China sea. *Geophys. Res. Lett.*, **35**, https://doi.org/10.1029/2008GL035520.

Stastna, M., and K. G. Lamb, 2002: Large fully nonlinear internal solitary waves: The effect of background current. *Phys. Fluids*, **14**, 2987–2999, https://doi.org/10.1063/1.1496510.

Stigebrandt, A., and J. Aure, 1989: Vertical mixing in basin waters of fjords. *J. Phys. Oceanogr.*, **19**, 917–926, https://doi.org/10.1175/1520-0485(1989)019<0917:VMIBWO>2.0.CO;2.

Stive, M. J., 1984: Energy dissipation in waves breaking on gentle slopes. *Coast. Eng.*, **8**, 99–127, https://doi.org/10.1016/0378-3839(84)90007-3.

Thornton, E. B., and R. Guza, 1983: Transformation of wave height distribution. *J. Geophys. Res.*, **88**, 5925–5938, https://doi.org/10.1029/JC088iC10p05925.

Thorpe, S., 1997: On the interactions of internal waves reflecting from slopes. *J. Phys. Oceanogr.*, **27**, 2072–2078, https://doi.org/10.1175/1520-0485(1997)027<2072:OTIOIW>2.0.CO;2.

Umeyama, M., and T. Shintani, 2006: Transformation, attenuation, setup, and undertow of internal waves on a gentle slope. *J. Waterw. Port Coast. Ocean Eng.*, **132**, 477–486, https://doi.org/10.1061/(ASCE)0733-950X(2006)132:6(477).

Venayagamoorthy, S. K., and O. B. Fringer, 2007: On the formation and propagation of nonlinear internal boluses across a shelf break. *J. Fluid Mech.*, **577**, 137–159, https://doi.org/10.1017/S0022112007004624.

Vlasenko, V., and K. Hutter, 2002: Numerical experiments on the breaking of solitary internal wavesover a slope–shelf topography. *J. Phys. Oceanogr.*, **32**, 1779–1793, https://doi.org/10.1175/1520-0485(2002)032<1779:NEOTBO>2.0.CO;2.

Walter, R. K., C. B. Woodson, R. S. Arthur, O. B. Fringer, and S. G. Monismith, 2012: Nearshore internal bores and turbulent mixing in Southern Monterey Bay. *J. Geophys. Res.*, **117**, C07017, https://doi.org/10.1029/2012JC008115.

——, M. E. Squibb, C. B. Woodson, J. R. Koseff, and S. G. Monismith, 2014: Stratified turbulence in the nearshore coastal ocean: Dynamics and evolution in the presence of internal bores. *J. Geophys. Res. Oceans*, **119**, 8709–8730, https://doi.org/10.1002/2014JC010396.

Waterhouse, A. F., J. A. Mackinnon, R. C. Musgrave, S. M. Kelly, A. Pickering, and J. Nash, 2017: Internal tide convergence and mixing in a submarine canyon. *J. Phys. Oceanogr.*, **47**, 303–322, https://doi.org/10.1175/JPO-D-16-0073.1.

Winters, K. B., P. N. Lombard, J. J. Riley, and E. A. D'Asaro, 1995: Available potential energy and mixing in density-stratified fluids. *J. Fluid Mech.*, **289**, 115–128, https://doi.org/10.1017/S002211209500125X.